



**Test Report on the November 2005  
NATO RTG-40 Active Imager Land Field Trials**

**by David Tofsted, David Quintis, Sean O'Brien, Jimmy Yarbrough,  
Manuel Bustillos, and Gail Tirrell Vaucher**

**ARL-TR-4010**

**December 2006**

## **NOTICES**

### **Disclaimers**

The findings in this report are not to be construed as an official Department of the Army position unless so designated by other authorized documents.

Citation of manufacturer's or trade names does not constitute an official endorsement or approval of the use thereof.

Destroy this report when it is no longer needed. Do not return it to the originator.

# **Army Research Laboratory**

White Sands Missile Range, NM 88002-5501

---

**ARL-TR-4010****December 2006**

---

## **Test Report on the November 2005 NATO RTG-40 Active Imager Land Field Trials**

**David Tofsted, David Quintis, Sean O'Brien, Jimmy Yarbrough,  
Manuel Bustillos, and Gail Tirrell Vaucher**  
*Computational Information Sciences Directorate, ARL*

<b>REPORT DOCUMENTATION PAGE</b>			<i>Form Approved</i> <i>OMB No. 0704-0188</i>	
Public reporting burden for this collection of information is estimated to average 1 hour per response, including the time for reviewing instructions, searching existing data sources, gathering and maintaining the data needed, and completing and reviewing the collection information. Send comments regarding this burden estimate or any other aspect of this collection of information, including suggestions for reducing the burden, to Department of Defense, Washington Headquarters Services, Directorate for Information Operations and Reports (0704-0188), 1215 Jefferson Davis Highway, Suite 1204, Arlington, VA 22202-4302. Respondents should be aware that notwithstanding any other provision of law, no person shall be subject to any penalty for failing to comply with a collection of information if it does not display a currently valid OMB control number. <b>PLEASE DO NOT RETURN YOUR FORM TO THE ABOVE ADDRESS.</b>				
<b>1. REPORT DATE (DD-MM-YYYY)</b> December 2006		<b>2. REPORT TYPE</b> Final		<b>3. DATES COVERED (From - To)</b> 2006
<b>4. TITLE AND SUBTITLE</b> Test Report on the November 2005 NATO RTG-40 Active Imager Land Field Trials			<b>5a. CONTRACT NUMBER</b>	
			<b>5b. GRANT NUMBER</b>	
			<b>5c. PROGRAM ELEMENT NUMBER</b>	
<b>6. AUTHOR(S)</b> David Tofsted, David Quintis, Sean O'Brien, Jimmy Yarbrough, Manuel Bustillos, and Gail Tirrell Vaucher			<b>5d. PROJECT NUMBER</b>	
			<b>5e. TASK NUMBER</b>	
			<b>5f. WORK UNIT NUMBER</b>	
<b>7. PERFORMING ORGANIZATION NAME(S) AND ADDRESS(ES)</b> U.S. Army Research Laboratory Computational and Information Sciences Directorate Battlefield Environment Division (ATTN: AMSRD-ARL-CI-EE) White Sands Missile Range, NM 88002-5501			<b>8. PERFORMING ORGANIZATION REPORT NUMBER</b>  ARL-TR-4010	
<b>9. SPONSORING/MONITORING AGENCY NAME(S) AND ADDRESS(ES)</b> U.S. Army Research Laboratory 2800 Powder Mill Road Adelphi, MD 20783-1145			<b>10. SPONSOR/MONITOR'S ACRONYM(S)</b>	
			<b>11. SPONSOR/MONITOR'S REPORT NUMBER(S)</b>  ARL-TR-4010	
<b>12. DISTRIBUTION/AVAILABILITY STATEMENT</b> Approved for public release; distribution is unlimited.				
<b>13. SUPPLEMENTARY NOTES</b>				
<b>14. ABSTRACT</b> The NATO Research Technology Group 40 (RTG-40) was established in 2003 to develop improved models of active imaging system performance to include the effects of atmospheric optical turbulence. Supporting the development of these models is the performance of naval and land field trials to provide data bases of system performance under varying turbulence conditions. In support of the land trials, the U.S. Army Research Laboratory's (ARL) Computational and Informational Sciences Directorate's Battlefield Environment Division (CISD/BED) provided extensive instrumentation as well as range sponsorship and coordination of the measurement program. This report documents the major accomplishments by the ARL group in preparation for and during the trials. The experiment was conducted at and sponsored by the High Energy Laser Systems Test Facility, located on White Sands Missile Range, NM. The test occurred 7-18 November, 2005. Weather conditions were typical for a southern NM in November; with temperatures ranging between 0-30 °C, variable winds, and clear to moderate cloud cover. Data were collected during four lasing periods spanning morning or evening neutral events, with additional passive data collected whenever possible. Data collected by the ARL team included 20 Hz U-V-W wind speed and temperature data from 4 RM Young sonic anemometers mounted at 2.5, 4.5, 6.5, and 8.5 m heights on a mid-range met tower, and 2/3 Hz turbulence ( $C_n^2$ ) data collected by 4 sets of Lockheed scintillometers set up in pairs (one at 2 m AGL, the other at 4 m) two pairs measuring between 0 and 1 km and another pair between 1 and 2 km. In this report we describe the instrumentation, the test, the data collected, and discuss the initial analysis performed on the meteorological data collected.				
<b>15. SUBJECT TERMS</b> Turbulence, scintillometer, active imagers, surface layer, characterization				
<b>16. SECURITY CLASSIFICATION OF:</b>			<b>17. LIMITATION OF ABSTRACT</b>  SAR	<b>18. NUMBER OF PAGES</b>  75
<b>a. REPORT</b> U	<b>b. ABSTRACT</b> U	<b>c. THIS PAGE</b> U		
			<b>19b. TELEPHONE NUMBER (Include area code)</b> (505) 678-3039	

---

## Contents

---

<b>List of Figures</b>	<b>v</b>
<b>List of Tables</b>	<b>vii</b>
<b>Preface</b>	<b>viii</b>
<b>Acknowledgments</b>	<b>ix</b>
<b>Executive Summary</b>	<b>xi</b>
<b>1. Introduction</b>	<b>1</b>
<b>2. The Field Trials</b>	<b>10</b>
2.1 Test Documentation .....	10
2.2 NATO Participants and Their Equipment .....	11
2.3 HELSTF Access .....	13
2.4 Test Logistics .....	13
2.5 Site Layout, Maps, and Tables .....	14
2.6 Test Day Planning .....	23
2.7 Post-Test Activities .....	25
<b>3. Initial ARL Data Analysis</b>	<b>25</b>
3.1 Data Acquisition.....	26
3.2 Computing Mean and Second Order Statistics.....	27
3.3 Temperature Corrections.....	30
3.4 Turbulence.....	33
3.5 Second Order Statistics .....	35
<b>4. Temperature and Wind Spectra and Turbulence Computations</b>	<b>42</b>
<b>5. Conclusion</b>	<b>51</b>
<b>References</b>	<b>52</b>

<b>Appendix: Scintillometer Calibrations</b>	<b>53</b>
<b>Acronyms and Abbreviations</b>	<b>55</b>
<b>Distribution List</b>	<b>58</b>

---

## List of Figures

---

Figure 1. Main test participants from ARL and RTG-40. Not shown are HELSTF and WSMR personnel. ....	1
Figure 2. Main downrange test area including observation area, and backstopping target berm at 2 km. ....	3
Figure 3. Targets used at 1 km (above) and 2 km, including 8'×8' registration target (lower left), 3-D targets (right), resolution patterns (center), and “eye chart” (above left). ....	4
Figure 4. Line of tents sheltering main imagers. From left-to-right are the Canadian ELVISS, Canadian LASSIE, Canadian high speed imager, German high speed imager, Swedish Gated Imager, U.K. Burst Illumination Laser (BIL), Danish BIL, and U.S. NVESD Active Short Wavelength Infrared (SWIR) systems. ....	5
Figure 5. 9 m ARL tower used during testing. ....	7
Figure 6. Two kilometer (2 km) scintillometers. ARL 2 m scintillometer is on scaffold at left. ARL 4 m scintillometer is at second level of scaffold at right. German scintillometer is on white tripod at left center. ....	8
Figure 7. One-half kilometer (½ km) Sensors, including Canadian meteorological mast with Metek sonic anemometer, prop and vane anemometer, and hygrometer. HELSTF meteorological tower with two-dimensional (2-D) sonic anemometers at 4 m and 8 m is shown in background. ....	9
Figure 8. RTG-40 site map showing site area groupings. The north direction is upward and positive, and the eastward direction is to the right and positive. ....	16
Figure 9. OA site group. System locations are surveyed as displacements along a line, anchored at the location of the Danish system (DASYS). ....	17
Figure 10. 500 M site area map. Circles around locations depict approximate uncertainty in the GPS measurements (approximately 5 m). ....	18
Figure 11. 1 KM site area map. Rectilinear coordinates on this and all other maps in this section are referenced to the same origin, which is located near the DASYS location at the observation area. ....	19
Figure 12. 2 KM target area site map. The 2KSCAFFOLD point is located on the top of a berm that backstops this target area. ....	20
Figures 13 and 14. Fifteen-minute mean horizontal wind speeds during November 9 <sup>th</sup> and 10 <sup>th</sup> for 2.5, 4.5, 6.5, 8.5 m sonic anemometer levels. ....	28
Figures 15 and 16. Fifteen-minute mean horizontal wind speeds during November 11 <sup>th</sup> and 12 <sup>th</sup> for 2.5, 4.5, 6.5, 8.5 m sonic anemometer levels. ....	28
Figures 17 and 18. Fifteen-minute mean horizontal wind speeds during November 13 <sup>th</sup> and 14 <sup>th</sup> for 2.5, 4.5, 6.5, 8.5 m sonic anemometer levels. ....	28
Figures 19 and 20. Fifteen-minute mean horizontal wind speeds during November 15 <sup>th</sup> and 16 <sup>th</sup> for 2.5, 4.5, 6.5, 8.5 m sonic anemometer levels. ....	29
Figures 21 and 22. Fifteen-minute mean horizontal wind speeds during November 17 <sup>th</sup> and 18 <sup>th</sup> for 2.5, 4.5, 6.5, 8.5 m sonic anemometer levels. ....	29
Figures 23 and 24. Fifteen-minute mean temperature plots for November 9 <sup>th</sup> and 10 <sup>th</sup> for 2.5, 4.5, 6.5, 8.5 m sonic anemometer levels. ....	31
Figures 25 and 26. Fifteen-minute mean temperature plots for November 11 <sup>th</sup> and 12 <sup>th</sup> for 2.5, 4.5, 6.5, 8.5 m sonic anemometer levels. ....	31
Figures 27 and 28. Fifteen-minute mean temperature plots for November 13 <sup>th</sup> and 14 <sup>th</sup> for 2.5, 4.5, 6.5, 8.5 m sonic anemometer levels. ....	32

Figures 29 and 30. Fifteen-minute mean temperature plots for November 15 <sup>th</sup> and 16 <sup>th</sup> for 2.5, 4.5, 6.5, 8.5 m sonic anemometer levels. ....	32
Figures 31 and 32. Fifteen-minute mean temperature plots for November 17 <sup>th</sup> and 18 <sup>th</sup> for 2.5, 4.5, 6.5, 8.5 m sonic anemometer levels. ....	32
Figures 33 and 34. Fifteen-minute mean turbulence plots for November 9 <sup>th</sup> and 10 <sup>th</sup> for 4 scintillometers.....	33
Figures 35 and 36. Fifteen-minute mean turbulence plots for November 11 <sup>th</sup> and 12 <sup>th</sup> for 4 scintillometers.	34
Figures 37 and 38. Fifteen-minute mean turbulence plots for November 13 <sup>th</sup> and 14 <sup>th</sup> for 4 scintillometers.	34
Figures 39 and 40. Fifteen-minute mean turbulence plots for November 15 <sup>th</sup> and 16 <sup>th</sup> for 4 scintillometers.	34
Figures 41 and 42. Fifteen-minute mean turbulence plots for November 17 <sup>th</sup> and 18 <sup>th</sup> for 4 scintillometers.	35
Figures 43 and 44. Fifteen-minute mean parameter plots for November 9 <sup>th</sup> and 10 <sup>th</sup> for 2.5 m level. ....	36
Figures 45 and 46. Fifteen-minute mean parameter plots for November 11 <sup>th</sup> and 12 <sup>th</sup> for 2.5 m level. ....	36
Figures 47 and 48. Fifteen-minute mean parameter plots for November 13 <sup>th</sup> and 14 <sup>th</sup> for 2.5 m level. ....	36
Figures 49 and 50. Fifteen-minute mean parameter plots for November 15 <sup>th</sup> and 16 <sup>th</sup> for 2.5 m level. ....	37
Figures 51 and 52. Fifteen-minute mean parameter plots for November 17 <sup>th</sup> and 18 <sup>th</sup> for 2.5 m level. ....	37
Figures 53 and 54. Fifteen-minute mean vertical momentum fluxes for November 9 <sup>th</sup> and 10 <sup>th</sup> for 2.5, 4.5, 6.5, 8.5 m sonic anemometer levels. ....	38
Figures 55 and 56. Fifteen-minute mean vertical momentum fluxes for November 11 <sup>th</sup> and 12 <sup>th</sup> for 2.5, 4.5, 6.5, 8.5 m sonic anemometer levels. ....	38
Figures 57 and 58. Fifteen-minute mean vertical momentum fluxes for November 13 <sup>th</sup> and 14 <sup>th</sup> for 2.5, 4.5, 6.5, 8.5 m sonic anemometer levels. ....	38
Figures 59 and 60. Fifteen-minute mean vertical momentum fluxes for November 15 <sup>th</sup> and 16 <sup>th</sup> for 2.5, 4.5, 6.5, 8.5 m sonic anemometer levels. ....	39
Figures 61 and 62. Fifteen-minute mean vertical momentum fluxes for November 17 <sup>th</sup> and 18 <sup>th</sup> for 2.5, 4.5, 6.5, 8.5 m sonic anemometer levels. ....	39
Figures 63 and 64. Fifteen-minute averaged sensible heat fluxes for November 9 <sup>th</sup> and 10 <sup>th</sup> for 2.5, 4.5, 6.5, 8.5 m sonic anemometer levels. ....	40
Figures 65 and 66. Fifteen-minute averaged sensible heat fluxes for November 11 <sup>th</sup> and 12 <sup>th</sup> for 2.5, 4.5, 6.5, 8.5 m sonic anemometer levels. ....	40
Figures 67 and 68. Fifteen-minute averaged sensible heat fluxes for November 13 <sup>th</sup> and 14 <sup>th</sup> for 2.5, 4.5, 6.5, 8.5 m sonic anemometer levels. ....	41
Figures 69 and 70. Fifteen-minute averaged sensible heat fluxes for November 15 <sup>th</sup> and 16 <sup>th</sup> for 2.5, 4.5, 6.5, 8.5 m sonic anemometer levels. ....	41
Figures 71 and 72. Fifteen-minute averaged sensible heat fluxes for November 17 <sup>th</sup> and 18 <sup>th</sup> for 2.5, 4.5, 6.5, 8.5 m sonic anemometer levels. ....	41
Figures 73 through 96. Hourly 15-minute-integration spectra of horizontal (u, red) and vertical (w, orange) wind, and temperature (blue) fluctuations of 9 November.....	50



---

## List of Tables

---

Table 1. GPS (WGS 84) coordinates and derived local rectilinear (X-Y) coordinates for the observation area relative to a fixed origin of latitude $X_0=32^{\circ} 38' N$ and longitude $Y_0=106^{\circ} 20' W$ .....	21
Table 2. GPS and derived rectilinear coordinates for the 500 M target and control area relative to a fixed origin of latitude $X_0=32^{\circ} 38' N$ and longitude $Y_0=106^{\circ} 20' W$ . ....	21
Table 3. GPS and rectilinear coordinates for location points at the 1 KM target area relative to a fixed origin of latitude $X_0=32^{\circ} 38' N$ and longitude $Y_0=106^{\circ} 20' W$ .....	21
Table 4. GPS and rectilinear coordinates for locations within the 2 KM target area relative to a fixed origin of latitude $X_0=32^{\circ} 38' N$ and longitude $Y_0=106^{\circ} 20' W$ .....	22
Table 5. Description key for site location labels.....	22
Table A-1. Alignment drift for each sensor.....	54

---

## Preface

---

In the spring of 2004 Army Research Laboratory (ARL) personnel were contacted by representatives of NATO Research Technology Group 40 (RTG-40) to discuss involvement in their mission to develop models to characterize the performance of active imaging systems. These systems represent a next generation of capability for military field sensors, including the capability of defeating camouflage systems through the use of active range-gated imaging. Swedish researchers spearheaded the use of this technology, where targets may be discriminated from backgrounds by range stepping an imager “through” the target to generate a three-dimensional concept of the battlefield.

The promise of such systems is to some extent compromised by the presence of atmospheric optical turbulence in the near surface atmosphere. Turbulence causes the illumination pulses of these systems to experience various deleterious effects: wave front distortion, time of arrival fluctuations, and scintillation. On the return path, the reflected energy is subject to further atmospheric distortion. While various system parameters may be varied to determine the optimal means of mitigating these effects, without actually building multiple systems with varying system parameters (a very expensive process), the alternative is the development of physics and engineering models to simulate atmospheric impacts on system performance. To validate such models databases of measurements under various turbulence conditions are required. The NATO RTG-40 objective of land and sea trials addressed this requirement by providing databases of conditions and propagation results for comparison with models. The White Sands Missile Range, New Mexico, situated in the Chihuahuan desert, provided a useful setting for such measurements. Turbulence levels measured during testing varied over two decades in magnitude during the course of the measurements program.

---

## Acknowledgments

---

Appreciation is extended to the many people who facilitated this test, including both local support, outside ARL staff, Strategic Missile Defense Command's High Energy Laser Systems Test Facility (SMDC/HELSTF), and the North Atlantic Treaty Organization (NATO) nation staffs and the Night Vision and Electronic Sensors Directorate (NVESD) who supplied the active imagers needed to perform the imaging component of the testing. From the White Sands Missile Range (WSMR) staff, we wish to particularly acknowledge Mike Hart, the radiation safety officer, Robert Floyd, range coordination, and Marc Chavez, flight safety officer. From the HELSTF there were many seen and unseen people who supported us, but we especially wish to thank first Mr. Thomas Hodge, HELSTF manager, and Mr. William Sutton, MOA liaison, without whose assistance the measurements would not have taken place. Additionally, we wish to particularly thank Mr. Stan East, whose tireless assistance aided immensely in smoothing the way to crossing a number of administrative hurdles. We also thank the HELSTF meteorological team (Tim Chavez and Frank Robitaille), whose instrumentation aided greatly in the characterization work. The safety crew were highly professional as well, including Rob Ognan and Bob Street on the measurement line as well as Mike Blondell in the control booth, Scott McKay in safety training, and Gary Wilson, who solidified our ground safety plan. There was also the electrical crew who restored power to the downrange area after a lightning strike a few weeks prior to the test. Their assistance, though in obscurity, was vital to a successful test.

We were also assisted significantly by the people at the ARL Survivability/Lethality Analysis Directorate (SLAD) Electro-Optical Vulnerability Analysis Facility (EOVAF): Norm Comer, chief, and Dave Bromley. They provided critical supplies for the operation of the optics and scintillometers.

Aside from the authors named, we also need to thank many ARL staff who contributed significantly to the success of this experiment. We thank the following from ARL for participating as foreign escorts Sean D'Arcy, Terry Jameson, Doyle "Scott" Elliott, SFC Robert Brice, John Raby, and Dr. David Marlin. Finally, we were ably assisted in various administrative details by our program analyst Linda Duchow, purchasing agent Felipe Chavez, supply officers Mike Mason and Rick Hanson, safety officer Felicia Chamberlain, and security chief Joseph Trammel. Lastly, we wish to thank the support of Drs. Don Hoock, Rick Shirkey, and Ed Measure, who helped us clear key administrative hurdles, and Saba (Lou) Lucas who provided a valuable review of the (near-final) document.

INTENTIONALLY LEFT BLANK.

---

## Executive Summary

---

The North Atlantic Treaty Organization (NATO) Research Technology Group 40 (RTG-40) was established in 2003 with the mandate to improve models of active imaging systems currently being developed by several NATO nations. The operation of these systems involves essentially three components: a pulsing laser, a range gating imager, and associated computer control equipment to integrate the laser and imager responses. The laser source pulses are switched so that they are only a few feet long. These pulses travel downrange to a target, reflect, and travel back to a range-gating receiver. This receiver, depending on the accuracy, can determine the range to each pixel in the image by varying the range gate (delay timing) electronically. With a complete three-dimensional (3-D) picture of the target region, even camouflaged targets can be discriminated from background by studying their 3-D structure. Such systems would be relatively simple to model, except for the ubiquitous optical turbulence in the surface boundary layer atmosphere.

Due to turbulence, the propagated downrange pulse becomes scintillated (varying illumination pattern) when it arrives at the target surface. The scintillated pattern is then reflected back through the atmosphere that can further blur the image. To model the effects of this scintillation, one must consider the vertical and temporal structures of the turbulent atmosphere. These scintillation effects are primarily due to localized temperature fluctuations. The greater the degree of diurnal variations in temperature, the greater will be the effects of the turbulence. Hence, White Sands Missile Range (WSMR), NM, located in the heart of the southwestern U.S. Chihuahuan desert, featuring daily diurnal temperature variations of as high as 40 degrees Fahrenheit, was viewed as a prime location for study of turbulence effects on active imaging systems.

The RTG-40 Active Imager Land Field Trials were performed in November 2005 at the High Energy Laser Systems Test Facility (HELSTF) located on the WSMR range. HELSTF was chosen because it provides a well-instrumented range specifically tailored to measure optical turbulence effects. Data collected by HELSTF during the experiments was included in the database of conditions developed by RTG-40. HELSTF's downrange test area also provided an area with existing instrumentation and hard power suitable for performing the trials both from safety and security viewpoints.

The data collected by Army Research Laboratory (ARL) during the experiments will be useful in a number of applications. First, it will be used in conjunction with the imagery data collected during the experiments. Second, this database consists of correlated tower and scintillometer data. The scintillometer data includes four pairs of scintillometers set up at 2 meters (m) and 4 m above ground level (AGL) over the first and second kilometers (0–1 and 1–2) of the path. These sensors completely characterize the propagation path. The objective was to permit

intercomparison of turbulence strength ( $C_n^2$ ) measured simultaneously as a function of height. The mean turbulence strength can then be intercompared, as well as the correlation of closely spaced paths. Meteorological wind and temperature data collected from the “met” tower set up mid-range can then be intercompared with the  $C_n^2$  data to determine the ability to predict turbulence strength based on micrometeorological variations. In this report the test is described and a preliminary data analysis is discussed.

---

## 1. Introduction

---

The North Atlantic Treaty Organization (NATO) Research Technology Group 40 (RTG-40) was established in 2003 to develop improved models of active imaging systems. A key objective of this group was to perform field trials of both land and naval systems. The key U.S. participants in this group were initially with the Communications Electronics Research Development and Engineering Command (CERDEC) Night Vision and Electronic Sensors Directorate (NVESD) from Fort Belvoir, VA. However, in the spring of 2004 David Tofsted of the U.S. Army Research Laboratory (ARL) was invited to participate in a meeting of RTG-40 held in Panama City, FL. The purpose of this meeting was to discuss the substance of the land field trials and develop a plan for their conduct. The plan was to include both the optics measurements to be performed during the trials and the placement and approach to site characterization of the strength and structure of turbulence during the measurement periods. The final list of participants included researchers from ARL, NVESD, the Air Force Research Laboratory (AFRL), researchers from the NATO countries Canada, the United Kingdom (U.K.), Denmark, Germany, and France, as well as the NATO Partnership for Peace nation Sweden. Over 75 personnel were involved, including direct participants (figure 1) and High Energy Laser Systems Test Facility (HELSTF) and White Sands Missile Range (WSMR) supporting staff.



Figure 1. Main test participants from ARL and RTG-40. Not shown are HELSTF and WSMR personnel.

An open question, initially, was where to locate the trials. Three potential sites for the land trials were proposed: WSMR, NM, Eglin Air Force Base, FL, and Fort Hunter Liggett, CA. Surveys of these three sites were made in the fall of 2004, the WSMR site survey was organized by David Tofsted. There were several beneficial features about HELSTF as the best choice. ARL and HELSTF have an existing memorandum of agreement (MOA) that was developed and has been supported for the past five years by ARL liaison Gail Vaucher and HELSTF liaison William

Sutton. The required agencies are in place and easily accessible for range coordination, safety and security. HELSTF has a high degree of safety and security control infrastructure built-in due to the sensitive nature of their site operations. The downrange area of HELSTF is well instrumented with in-situ meteorological sensors and is well-characterized by a good collection of historical measurement data. There is also considerable micro-turbulence measurement expertise available. Hard power is available at several downrange locations. There are fewer and shorter roadblocks to contend with than other choices considered and the terrain is flatter and drier. The HELSTF site and its support facilities are easily accessible from Highway (Hwy.) 70.

ARL personnel were instrumental in providing most of the logistical aspects of the RTG-40 test, including shipping and receiving of equipment from the various test participants, visitor support requirements, range coordination with both HELSTF, where the test occurred, and WSMR operations staff. As events unfolded, it became apparent that ARL had undertaken what appeared to be an ever-growing set of responsibilities in sponsoring the RTG-40 land field trials. A presentation of logistical aspects of the RTG-40 test is provided in section 2 and discussion of their progression in severity is provided in section 4 of this report.

The land field trials were performed in mid-November, 2005, at HELSTF. The week of 7–11 November was the setup week, with Monday morning devoted to badging and site orientation. Monday afternoon and Tuesday morning were spent setting up active imagers, Canadian meteorological sensors, and German scintillometers. U.S. ARL meteorological equipment had been set up in the three weeks prior to the testing period. The trials were performed in the region of HELSTF known as the downrange area. It consists of a 2-kilometer (km) fenced area northwest of the primary HELSTF cantonment area containing the Laser System Test Center (LSTC). The active imagers and supporting equipment were located along a line ‘front line’ just northwest of the LSTC fence noted as the 0-km site and commonly referred to as the ‘Observation Area’ (OA). The foreign visitors under ARL escort were restricted to the OA, the downrange area and the HELSTF cafeteria for security reasons. A schematic of the test area is shown in figure 2.



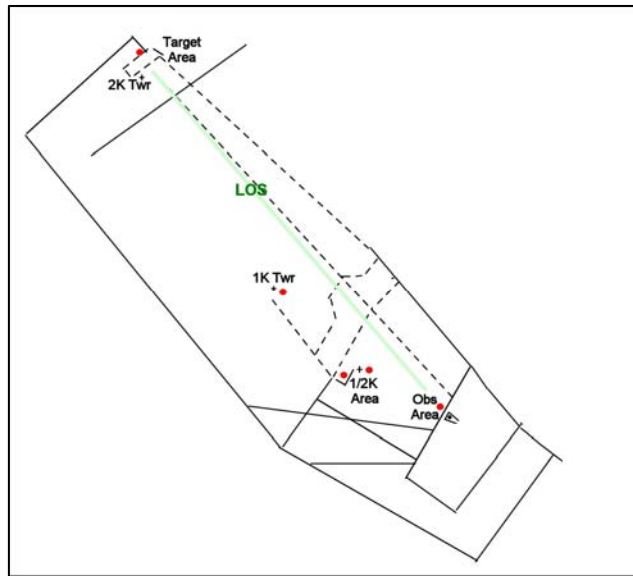


Figure 2. Main downrange test area including observation area, and backstopping target berm at 2 km.

By Tuesday afternoon nearly all the equipment was ready for registration testing. The primary issues were to ensure that the beams directed downrange would not leave the HELSTF range. To determine this, a downrange registration target had been constructed. The target consisted of an 8'×8' white-painted plywood panel, with registration markings at the target center consisting of 1 centimeter (cm) × 5 cm black stripes every 10 cm in both horizontal and vertical directions (refer to figure 3). At the 50 meter (m) downrange location, each 10 cm stripe separation would represent 2 millirad (mrad). Using this target each system was tested to determine the extent of its illumination beam. In particular, the Swedish gated imager system was a concern because its beam was a bright green. This beam was adjusted to lower the beam centroid so that it would fall below the level of the berm at 2 km for the full path testing. Similar adjustments were made for the other beams as well, though the other beams were all eye-safe after the first hundred meters. For convenience and safety purposes a series of three 10 by 20 foot (ft) tents were erected over the lasers so that if any should fall, the beam would be contained within the tent area. Also, use of the tents permitted test participants to stay behind and outside of the lasing enclosure; thus, not requiring protective eyewear whenever they were not operating their particular laser.

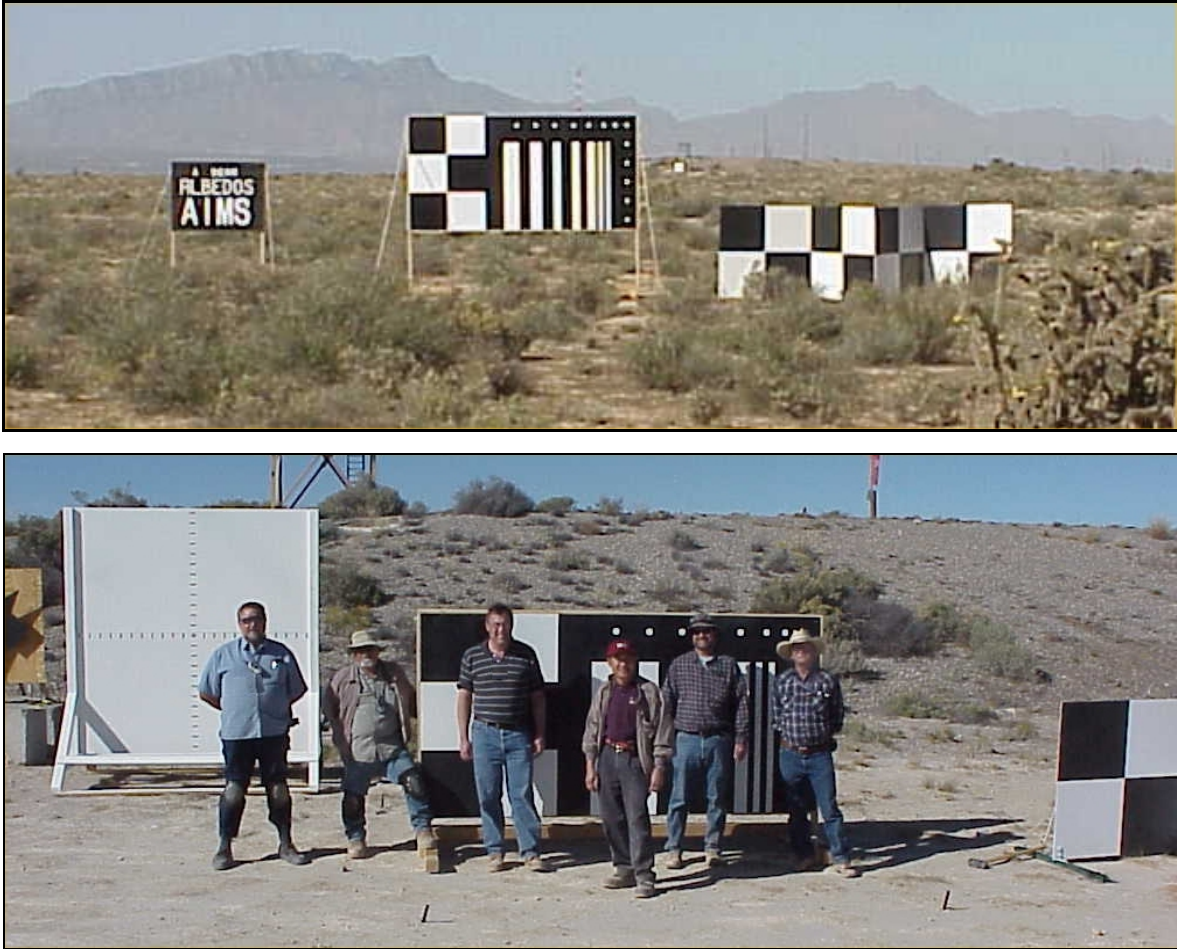


Figure 3. Targets used at 1 km (above) and 2 km, including 8'x8' registration target (lower left), 3-D targets (right), resolution patterns (center), and "eye chart" (above left).

Several additional target types are shown in figure 3. Each was designed to test a particular aspect of the active imaging system performance. During testing, each sensor would successively dwell on each target at 1 km and 2 km. This series could then be used to evaluate the performance of the sensor at different resolution tasks at different ranges and under different levels of optical turbulence. The line of laser imagers is shown in figure 4.



Figure 4. Line of tents sheltering main imagers. From left-to-right are the Canadian ELVISS, Canadian LASSIE, Canadian high speed imager, German high speed imager, Swedish Gated Imager, U.K. Burst Illumination Laser (BIL), Danish BIL, and U.S. NVESD Active Short Wavelength Infrared (SWIR) systems.

The testing phase occurred during the second week, November 14–18. Four testing periods were available, as dictated by other range missions and a missile flight safety plan, which stated that the proposed laser systems would be required to operate within a ceiling of 10,000 ft. Though we questioned this requirement, we were consequently not permitted to lase under several occasions when aircraft were in the area, even though our systems could not have caused laser hazards due to their very short hazard ranges, the presence of backstopping berms, and the use of the tents. Lasing operations were thus confined to four periods during the week: Monday morning, the 14<sup>th</sup>, from 0600–1000, Wednesday morning, the 16<sup>th</sup>, from 0500–0900 and from 1600–1900, and Thursday evening from 1700–2000. Measurements were also taken on Tuesday afternoon with the passive Canadian and German high speed cameras. Data were also taken on a regular basis by the Canadian and ARL meteorological sensors.

The systems present included the U.S. CERDEC NVESD Active Imager system and the U.K. Burst Illumination Laser (BIL) systems operating at 1570 nanometer (nm) wavelength, the Danish BIL and Swedish Gated Imager systems operating at 532 nm (green), and two Canadian systems operating in the near infrared (NIR) waveband (810 and 860 nm, respectively): ELVISS.

Enhanced Low light level and Visible Surveillance System (ELVISS) and Land-based Active System & Surveillance Image Enhancement (LASSIE). ELVISS was the more sophisticated of the systems, operating from a mounted tracking ball, ELVISS could be slewed by an operator using a joystick from inside the Canadian control van. ELVISS could also be controlled in various ways, including operation in passive mode and active modulation of its range gate, to select out objects at different general ranges. ELVISS is primarily a search and rescue type system, so one of the key areas of study for the Canadians was testing of a variable polarization reflecting material added to one of the standard targets. LASSIE was a prototype of an advanced version of ELVISS, with nearly the same wavelength and propagation characteristics as ELVISS, but without the same tracking or ranging capabilities. ELVISS and LASSIE were only operated

either just before sunrise or just after sunset during the test period, because they could not be operated under full sunlight.

The NVESD system experienced problems almost from the beginning of the test. It had apparently been damaged during an experiment in California the week before, because the laser never operated properly during the test period. The U.K. BIL also experienced problems during the setup week with its Intevac receiver. However, the U.K. staff took it “home” for the weekend and repaired it, using their hotel room as a working laboratory. The U.K. system was thus online for Monday morning. It also was available for the Wednesday morning data collections. On Wednesday evening, however, it experienced a problem with the cooling system in the laser. Coolant flooded the laser box and the system was disabled for the remainder of the test. We thus lost our remaining SWIR (Short-wave IR) band sensor midway through Wednesday night.

The remaining two sensors, the two visible systems, operated throughout the testing period. Though experimental systems, they performed well throughout. The Danish system worked particularly well under very low turbulence conditions. Its range gating capabilities allowed it to determine the range to downrange targets within a few millimeters. The Swedish gated imager, likewise, had range-gating capabilities, though it was designed to collect wider-angle images with a lower range step resolution.

Of the meteorological (“met”) equipment used to characterize the atmospheric turbulence conditions during the lasing events, ARL had a met tower at 1 km downrange. This tower had RM Young sonic anemometers set up at 2.5, 4.5, 6.5, and 8.5 m above ground level (AGL). Figure 5 shows a schematic of the tower (the tower was accidentally left out of the photographic records). These were set to sample U-V-W winds at 20 samples per second. Air temperature was also collected at these levels.

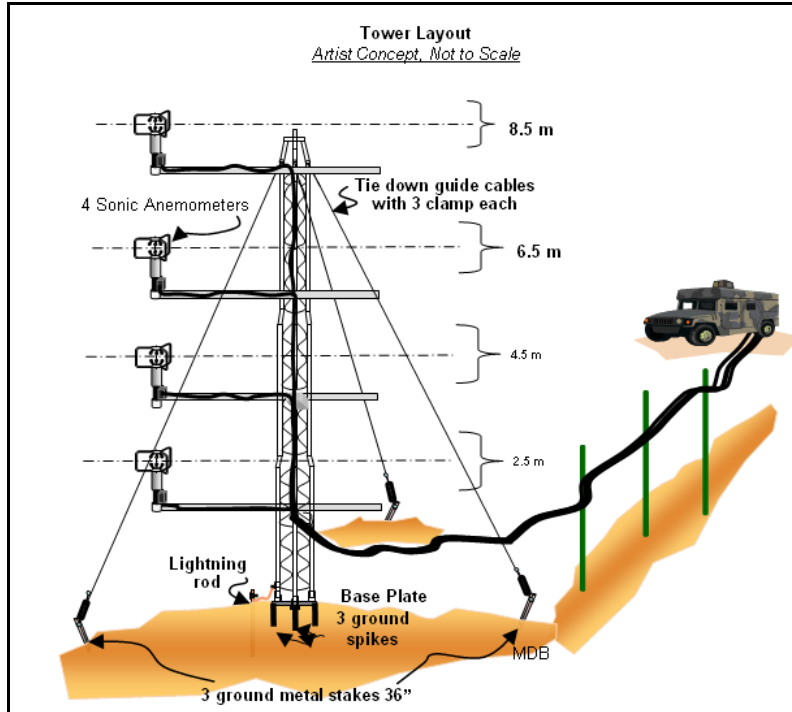


Figure 5. Nine meter (9 m) ARL tower used during testing.

A net solar radiation sensor was set up at the 1 km range on one of the scintillometer receiver scaffolds. ARL had four scintillometers set up to characterize the turbulence refractive index structure parameter ( $C_n^2$ , [ $\text{m}^{-2/3}$ ]) at 40 samples per minute. Two scintillometers were situated to characterize the 0–1 km portion of the optical path; the other two characterized the second kilometer of the 2 km path to the backstopping berm. For each scintillometer pair, one scintillometer was set up at 2 m AGL, the other at 4 m AGL. All four scintillometer receivers were located at the 1 km downrange area. To avoid interference between the different scintillometer signals, each pair (0–1 km and 1–2 km) was set up in a crossed beam pattern so that the centers of each beam pair would overlap the same terrain. Figure 6 shows the 2 km scintillometer setup. Because the scintillometer sine-squared path weighting function is maximal at the center of the path, this geometry permits the pair of beams to bear the greatest weight over the path segment.





Figure 6. Two kilometer (2 km) scintillometers. ARL 2 m scintillometer is on scaffold at left. ARL 4 m scintillometer is at second level of scaffold at right. German scintillometer is on white tripod at left center.

In addition to the ARL met equipment, the HELSTF range organization provided characterization data from their scintillometer, temperature, and wind equipment on their  $\frac{1}{2}$  km and 1 km met towers. Data were available at 10-second intervals throughout the measurement period. Data included 8 m and 32 m scintillometers, and temperature/wind data at 4, 8, 16, and 32 m. Canadian meteorological equipment included a 1.5 m mast located at 500 m downrange. Data collected from this mast included air temperature, wind, and humidity data. Figure 7 shows the Canadian mast and the lower portion of the  $\frac{1}{2}$  km HELSTF tower. During lasing periods, the Canadians also operated an SLS 20 type Scintec scintillometer. This scintillometer model is useful in obtaining inner scale measurements of the turbulence conditions. Their wind data were collected using a Metec sonic anemometer.

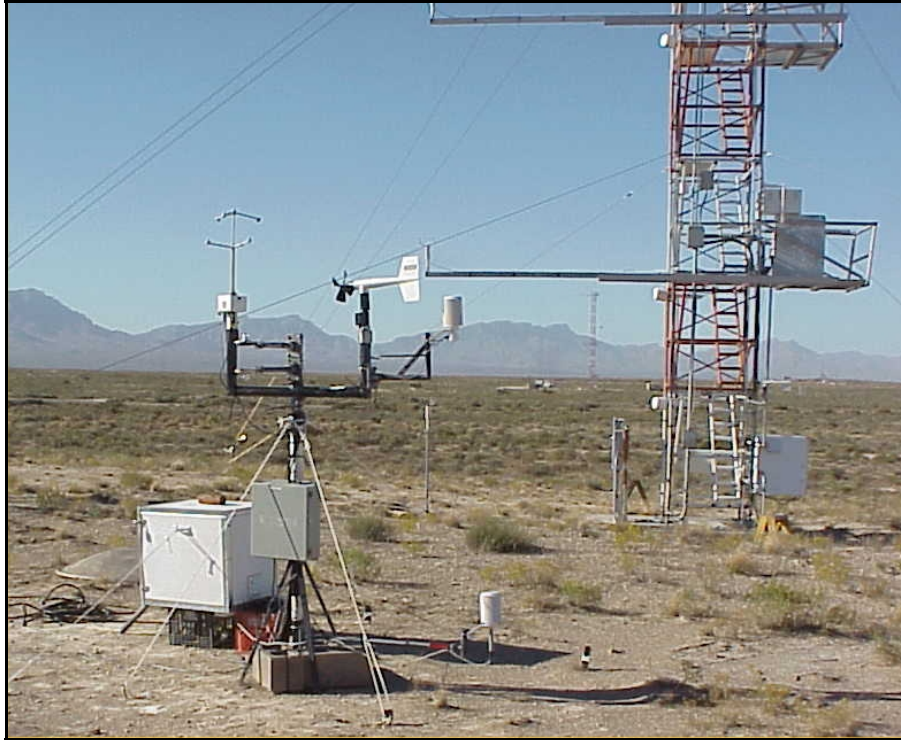


Figure 7. One-half kilometer ( $\frac{1}{2}$  km) Sensors, including Canadian meteorological mast with Metek sonic anemometer, prop and vane anemometer, and hygrometer. HELSTF meteorological tower with two-dimensional (2-D) sonic anemometers at 4 m and 8 m is shown in background.

The Germans also set up two Scintec BLS-900 scintillometers (see figure 6). Unfortunately, these experienced problems from the outset, with apparent malfunctions of one of the transmitters and one of the receivers. The setup period was extended through Thursday to attempt to bring these systems on line. Eventually, the German personnel were able to get a working scintillometer setup functioning between 0 and 1 km, virtually along the same line as the ARL 0–1 km sensors, but at a height of around 1.5 m AGL.

It had been hoped that we could collect met data throughout the measurement period with the available ARL instrumentation. However, because the observation area was forced to run on generator power, which was only available during lasing periods (when the OA site was occupied), we could only take several hours of data from the scintillometers originating from the 0 km point. Met data from the downrange towers, however, were available during nearly the complete period, except for short intervals where the sensors were taken offline to download data. Monitoring of the data collected also revealed difficulties with one of the 1–2 km scintillometers. When the turbulence passed through each neutral event, the scintillometer apparently could not properly track the low level turbulence present, though it seemed to operate appropriately during relatively high turbulence periods. Intermittent difficulties with the 6.5 m sonic sensor were also uncovered during post-test analysis, as will be shown below.

Overall, despite the few outages of equipment that normally occur during an effort of this scope, this is likely the best-instrumented field test of turbulence effects on both active and passive imaging systems in existence. Massive imagery data sets were collected and distributed to the various NATO partners in the experiment. The meteorological data sets were also distributed for correlation to the imagery data collected. The meteorological data sets themselves are being studied intently for their information regarding turbulence characterization. For years to come, these data sets will provide the means to examine properties of the nocturnal boundary layer and should prove useful in assessing the relative merits of various surface layer prediction and characterization methods. Many thanks are due to the persistence and perseverance of the many participants in this test whose dedication and contributions made this test possible.

---

## **2. The Field Trials**

---

In this section we present various issues and challenges that unfurled through the planning, pre-test, test and post-test phases of the land trials. In total, there were 23 foreign visitors, 4 USA visitors, 23 direct HELSTF participants, and 28 direct ARL participants for a total of 78 direct participants. There were many others indirectly involved, especially oversight agencies (road block, range engineering, range communication, Army sponsor, flight safety, frequency control) from WSMR.

### **2.1 Test Documentation**

A cyclic process of communication, correspondence, and coordination were required among ARL planners and various agencies to compose intermediate and finalized documents prior to the actual start of the RTG-40 land trials. Some of the documents composed in the planning phase included: the Laser Ground Safety (LGS) plan, the Missile Flight Safety (MFS) plan and the Operational Requirements Document (ORD).

The ‘Safety Operating Procedure (SOP) for the NATO RTG 40 Experiment’ was over 44 pages in length. This SOP included references to: existing Army Regulations (AR), training assertions, laser operator statement forms, location descriptions, map and location graphics, site layout descriptions, target descriptions and pictures, active imager descriptions with pictures, instrumentation and equipment layout descriptions, transmitter-receiver characteristics and safeguards, personal protective equipment (PPE), laser goggles, roadblock and barricade planning, emergency response plans and much more. Attached were appendices for: Test Schedule, List Of Participants (by sub groups), Test Participant Responsibilities (by sub groups) and Hazard Analysis Lists. To gain a sense of the complexity and extensive nature of this SOP a short (20% of the complete) list of topic phrases from the last SOP iteration follows:



- 1) verify check of entire line-of-sight (LOS) for potential reflective surfaces that could cause inadvertent specular reflections
- 2) check personnel jewelry that might cause inadvertent reflections
- 3) no reflective surfaces on targets (nail or screw heads)
- 4) how to control laser aperture to prevent lasing above 0 degrees elevation
- 5) how to control azimuth slew within backdrop berm area
- 6) potential hazardous range for each device
- 7) announcement procedure before each lase event
- 8) double verify laser alignment each time lase and switch to a new target
- 9) must cover not bury cable wiring
- 10) mark trip hazard and barrier tape personnel obstacles

Environmental impact issues and personnel hazard questions had to be addressed and some required documented solutions. The support vehicles, diesel generators and any equipment that contained fluids had to include double barrier drip containers on the ground. Fire extinguishers were located near the generators and personnel break tent near the OA. The entire downrange site had an abundance of cacti. The cactus plants at the OA site were delineated with bright yellow caution tape. The field of view immediately in front of the line of imagers, 50 ft downrange was outlined in bright yellow caution tape. All towers, tripods, guy wires, rope tie-downs and ground stakes included conspicuous indicator ribbons of yellow caution tape.

Also during the planning phase, a field test operations master plan was composed and disseminated showing each day's itinerary of test operations and escort-visitor schedules. During the test phase, these daily itineraries were updated to reflect necessary changes and briefed after the convoy arrival and group assembly at the OA.

## **2.2 NATO Participants and Their Equipment**

The amount of paperwork effort required to accommodate the participation by 23 foreign (and 4 USA) visitors in RTG-40 was prodigious. NATO/Partnership-for-Peace nations were required to obtain visas and complete the requisite paperwork to verify security credentials. There was continuing communication among ARL planning personnel and ARL, SMDC (HELSTF's headquarters element), and HELSTF security offices and visitors to complete visit request information and to ensure that all command organizations were in concurrence regarding the visitors' requests. Lists of attendees, POCs, and security information were updated beginning in the planning phase until just prior to personnel arrivals. Visitors were provided information and pertinent printed material on hotel, restaurants, and local points of interest as well as maps and route information.

The test support requests appeared in a continuous and persistent stream. Many test participants had ventured over long distances, so they not unreasonably relied on ARL and HELSTF to provide for all their logistical support needs. At times during the planning phase the ARL test director had to reprioritize the list of support topics in which some requests were deemed to be unnecessary luxuries. An example of a curtailed effort was ongoing research of costs to rent/lease vans, truck, and portable buildings. ARL provided two diesel generators to supply all power required at the OA. Additionally ARL made the arrangements for a diesel tanker supply truck to make two deliveries over the course of the test. In retrospect, ARL provided more power generation capacity at the OA than was actually required. Several visitors incorrectly estimated their power requirement to be one 120-volt circuit per plug. One visiting group originally requested that ARL provide a power output in their country's native standard rather than the differing 120/240-volt, 60 Hertz (Hz) American standard.

The logistical task of tracking and coordinating shipments of equipment in and out of country and the transfer of that equipment between WSMR and HELSTF was coordinated by Manny Bustillos. The general procedure was to receive visitor's equipment by commercial carrier at the ARL logistics location of building 1646 at WSMR. Each visiting group was required to plan and implement their equipment shipment procedures with the shipper of their choice. Some confusion resulted from shipments that were directed to the WSMR post receiving location rather than to ARL's separate receiving location. Each shipment received was documented regarding the visual description, amount, and condition of equipment. In order to transfer equipment from ARL logistics at WSMR to HELSTF, Mr. Bustillos would coordinate with the ARL logistics personnel to load the equipment on a flatbed and meet him at the HELSTF site entrance. He would then escort the equipment load to the OA if the owners were ready to receive it or to a secured indoor holding facility until such time that the owners were ready to receive it at the OA. Problems were not restricted to the incoming leg of equipment shipments. One of the shipments out of the U.S. was delayed in customs for several months due to a discrepancy in paperwork. ARL personnel intervened by having a military shipper resolve the issue.

The logistical task of providing food services was executed smoothly due to Mr. Bustillos' coordination efforts with the HELSTF cafeteria personnel. The HELSTF cafeteria personnel were very flexible and adaptive to the needs of the RTG-40 participants. They not only stocked up with additional provisions to handle the increased volume of personnel but also purchased foods that were appropriate to the cultural preferences of the visiting participants. Menu selections were adjusted to accommodate medical issues such as diabetes. A general menu with always-available food and snack selections was composed and handed out to visitor groups for their convenience of planning. On several occasions the cafeteria personnel opened early, stayed open late and extended standard dining hours to suite the scheduling needs of the RTG-40 personnel. ARL provided drinking water in insulated containers, bottled drinking water and, periodically, donuts at the OA.

There were several provisions made for restroom facilities. The HELSTF cafeteria had commercial grade restrooms. There were restroom facilities within the HELSTF facility compound by way of a valid escort at select times. Mr. Bustillos coordinated the efforts to set up portable units at the OA for the convenience of all field test participants.

### **2.3 HELSTF Access**

As a secure facility, HELSTF required that all personnel receive training on safety and security aspects of the site. HELSTF has various protocols for specific types of emergencies, particularly those related to unexploded ordinance on range. All ARL escort personnel received foreign visitor escort training and specialized safety training regarding the HELSTF site. Foreign visitors received an abbreviated training session on procedures to follow when on range. During the pre-test phase a dry run safety drill was performed to test the escort-visitor groups' knowledge of the appropriate cover areas, radio communications protocols, and evacuation timing issues.

### **2.4 Test Logistics**

For safety purposes (that is, in order to account for all personnel in case of the need to evacuate the site), personnel communication, conduct and movement within the HELSTF was closely monitored. The personnel tracking system that was devised also provided for increased accountability of foreign visitors, and allowed test supervisors to know the whereabouts of every person at any given time, in case they needed to be contacted for a request. We constructed a scheme where each ARL, U.S. visitor, or foreign national test participant was identified by a unique card from a standard playing card deck. This scheme was used in radio and on-site communications to enhance both clarity and brevity. The system worked well for escort-visitor grouping and location accountability of personnel. We tried to implement this approach so that there would be enough escorts to comfortably oversee all visitors. There was typically a ratio of one ARL escort to no more than about five visitors.

Prior to the start of each day's operations, all personnel met at the guard gate entrance to the HELSTF facility on HWY 70. The ARL escort personnel would show up early to receive their visitor assignments. The group assembly area was parking areas near the guard gate and the adjacent cafeteria facility. The orderly movement of personnel from the HELSTF entrance area to the AO was accomplished in a convoy fashion with ARL personnel in the lead and rear vehicles. This convoy method was also used when the group traveled between the AO and the cafeteria facility for lunch breaks and for the group egress at the end of each day's operations. The number of vehicles in the train was reduced by carpooling. Whenever one or more visitors required travel to a specific location in the downrange area in between lasing sessions, an ARL escort would accompany them. There were several key aspects to maintaining good communications. Communication among most groups in the field was accomplished using eight Family Radio Service (FRS) ½ watt walkie-talkies. Additionally, key HELSTF and ARL personnel had commercial grade radios for inter-communication between specific groups. These

groups included front-line safety and operations personnel, the HELSTF personnel in the command center, and ARL coordinators in a building at the 500 m site referred to as “Communications Central.” These ARL coordinators utilized a ‘playing field’ table representing a miniature mock-up of the downrange area. They updated (card suite and number) token positions to represent the site location of all personnel. So the communication announcement protocol for an operational status change or a personnel movement status change was to notify communications central with (1) identification (ID) of the caller, (2) status change message, and (3) ID of all other persons in immediate attendance.

Any off-road excursions in the downrange area required that a person walk in front of the vehicle noting possible hazards and guiding the vehicle driver safely around the hazard. General hazards included endangered flora and fauna, cacti, pot-holes, and the possibility of unexploded ordnance (UXO). At one point during the test week, two objects suspected of being UXO were sighted and subsequently disposed of by the UXO team. During the pre-test and test phase during lasing periods, personnel within the three 10’×20’ tents end-to-end covering the front line of active imagers wore laser goggles of the proper optical density (OD) rating. The back flaps of these tents were unfurled providing a barrier to the common “break tent” area behind the front line. To the immediate west of this front line was the ARL high-speed equipment trailer and to the immediate east of this front line was the Canadians’ instrument trailer.

## **2.5 Site Layout, Maps, and Tables**

During the course of the RTG-40 test, we used commercial grade Global Positioning System (GPS) personal receivers to mark the position of participating imager/camera systems, targets, meteorological sensors, support equipment, and shelter structures. We tried to get the best location accuracy possible by allowing sufficient time for individual GPS fixes to stabilize on the maximum number of available satellite signals and by averaging over multiple fixes. Generally speaking, we were able to obtain positional accuracies of the order of 16 ft (5 m) for the majority of our measurements. The 5 m error level is depicted (in approximation) as a circle around each GPS location point that is shown on the area detail maps below (figures 9–12).

Unfortunately, both of the ARL personnel who collected GPS information also served as escorts for foreign national personnel during the test. The GPS measurements were thus collected while waiting for foreign investigators to attend to their test equipment, and were frequently interrupted when these personnel moved to different locations. Target boards and some site characterization equipment were also moved to different sites on the test range over the course of the test, sometimes before GPS measurements could be made for the earlier location. As a result, the catalogue of GPS fix points is not comprehensive, but it is felt that only a few, less significant points of interest have been omitted.

One major problem was encountered with attempts to get accurate GPS fixes for sensor systems under the OA tent enclosure. Two sets of GPS location measurements were taken (on separate days) for these systems, and only the Danish visible band system (labeled as “DASYS” below)

showed any acceptable degree of repeatability. Most of the other system locations showed poor repeatability in absolute and relative (to other system) positioning. We are not certain about the source of this inconsistency, but we suspect that multipath reflections of the GPS signals of the thick metal tent skeleton or off of the sides of adjacent metal equipment trailers may have been at least partly responsible. As a work-around, we visited the site after the conclusion of the test and measured displacements of each system position along a baseline defined by the average GPS positions of the Danish system and the Canadian ELVISS system (which were on opposite ends of the line of systems at the OA). The GPS latitude-longitude coordinates were converted to a Cartesian (XY) system under a spherical earth assumption using the following relations:

$$X = \frac{2\pi R_E}{1.296 \times 10^6} (\alpha_D - \alpha) \cos \lambda$$

and

$$Y = \frac{2\pi R_E}{1.296 \times 10^6} (\lambda - \lambda_D),$$

where  $R_E = 6372.8$  km is the mean radius of the earth assumed here,  $1.296 \times 10^6 = 360 \times 3600$  is the number of arc seconds in a circle,  $(\lambda, \alpha)$  is the (latitude, longitude) of the given point, and  $(\lambda_D, \alpha_D)$  is the (latitude, longitude) of the first GPS fix that was taken for the location of the Danish system. Note that the longitude and latitude differences shown above are given in units of arc seconds.

Figure 8 shows an overview of the four major site groupings or “areas” for the RTG-40 site. Note that we have omitted height details from the map because the GPS height measurements had errors that frequently exceeded actual terrain height differences (which can be appreciated by careful examination of heights given in tables 1–4). The main LOS ran from the OA to the northwest. The meteorological sensors and support equipment shelters were generally clustered to the west or southwest of target locations within each target area.

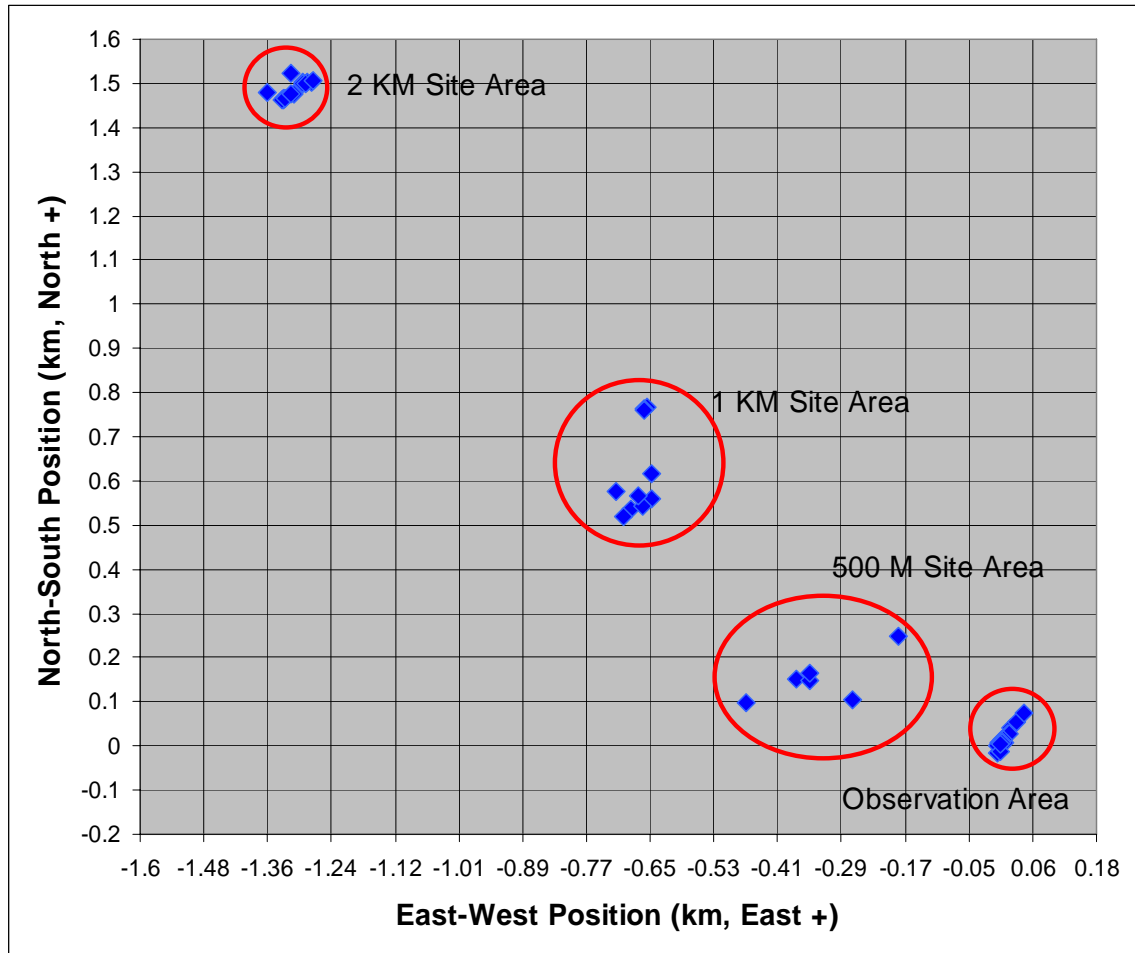


Figure 8. RTG-40 site map showing site area groupings. The north direction is upward and positive, and the eastward direction is to the right and positive.

Figure 9 shows the layout of the systems and support equipment at the OA. As previously mentioned, an alternate approach for determining the systems locations had to be used to rectify inaccurate GPS positional data.

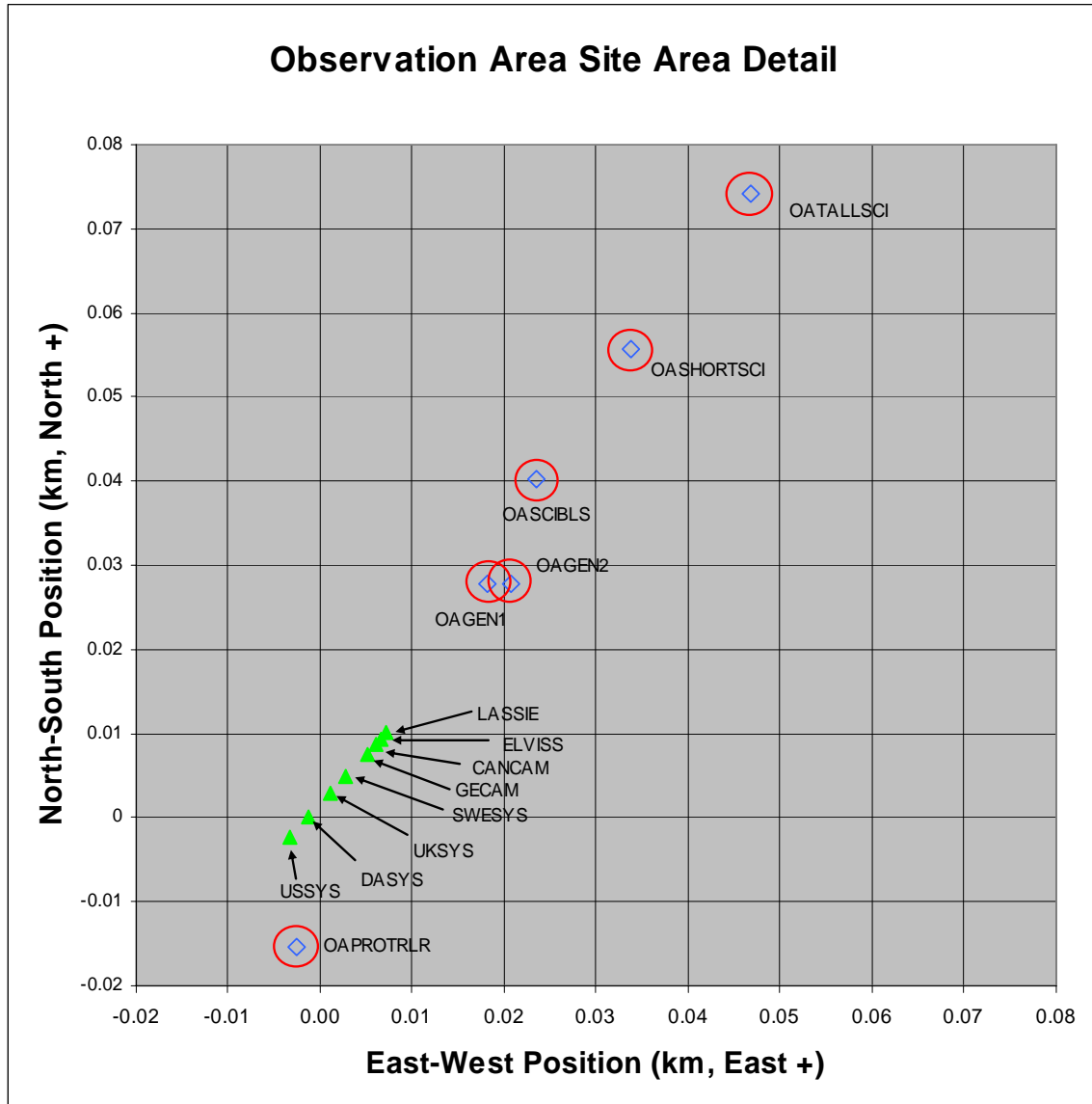


Figure 9. OA site group. System locations are surveyed as displacements along a line, anchored at the location of the Danish system (DASYs).

Figure 10 shows the layout of the 500 m target area, which had the shortest LOS to the OA systems. Only a few targets were set up at this location, primarily by the Canadian group.

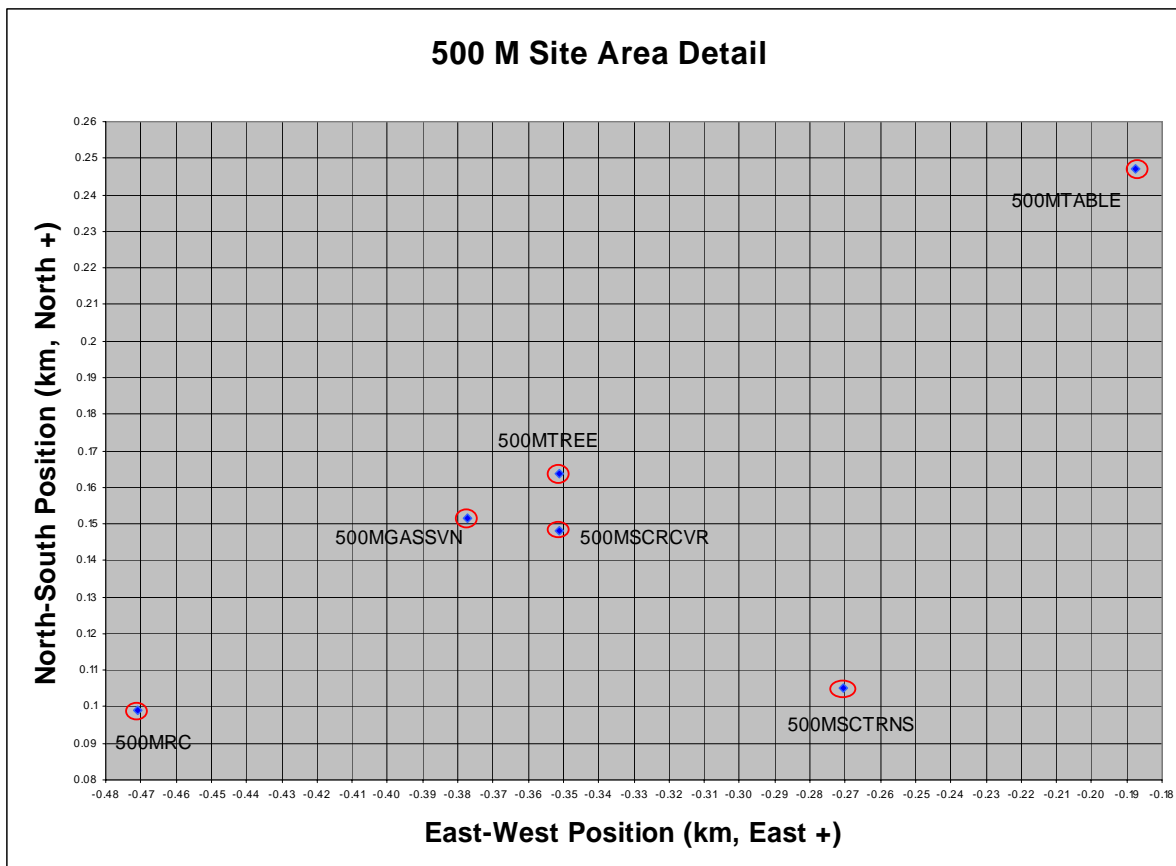


Figure 10. 500 M site area map. Circles around locations depict approximate uncertainty in the GPS measurements (approximately 5 m).

Figure 11 shows the layout of the 1 km target area, where many of the resolution targets used by the SWIR and visible band laser ranging systems were deployed.





The longest LOS range target site was at 2 km, which is depicted in figure 12. At both this and the 1 km site, HELSTF has installed permanent tall meteorological towers, upon which laser scintillometers are situated.

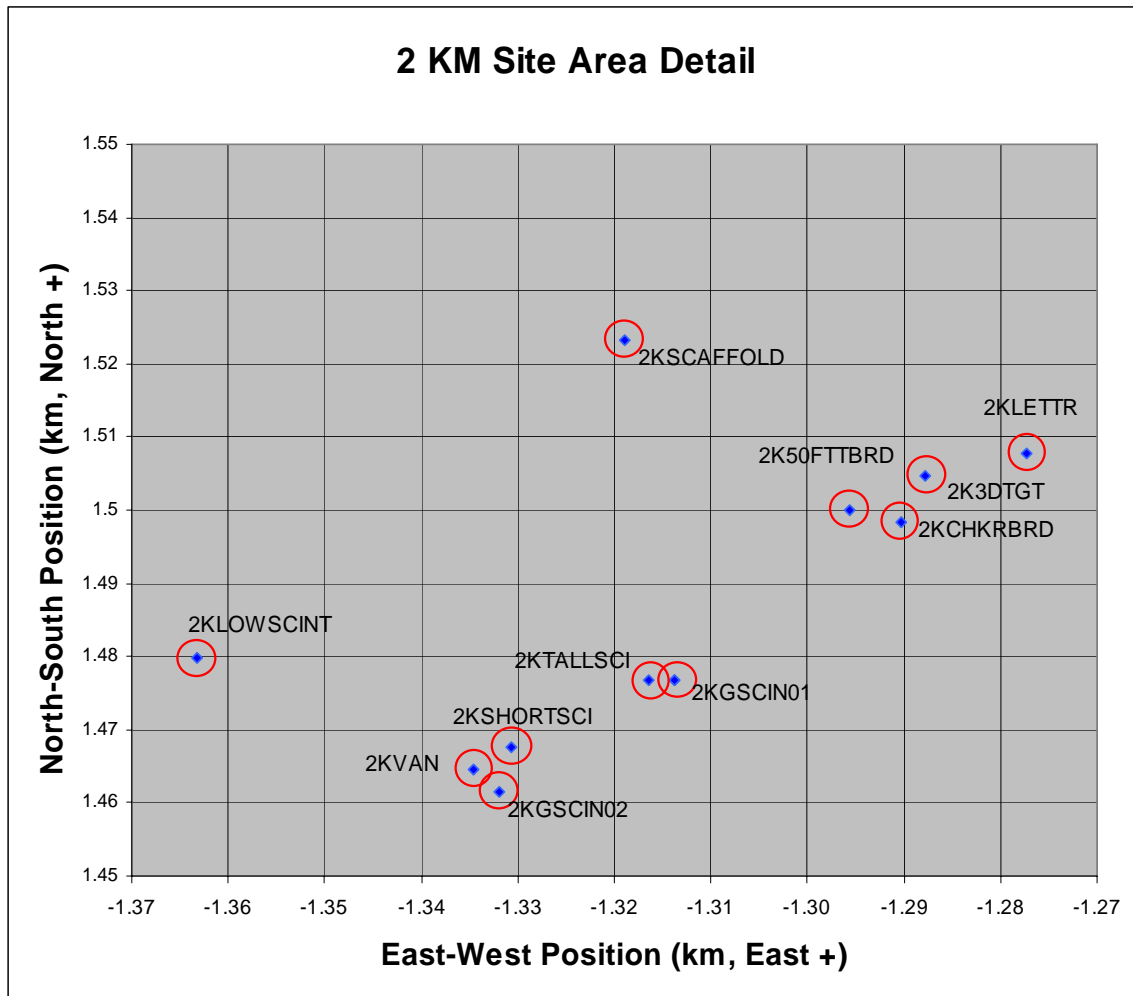


Figure 12. 2 KM target area site map. The 2KSCAFFOLD point is located on the top of a berm that backstops this target area.

Tables 1 through 4 contain the basic positional data that were used to construct the layout maps of figures 8–12. An explanation of labels that are used in figures 9–12 and tables 1–4 is contained in table 5.

Table 1. GPS (WGS 84) coordinates and derived local rectilinear (X-Y) coordinates for the observation area relative to a fixed origin of latitude X0=32° 38' N and longitude Y0=106° 20' W.

Point	Lat (X0+X'')	Lon (Y0+Y'')	Elev (ft)	Y-N (km)	X-E (km)	R (km)
USSYS				-0.00229	-0.00323	0.003965
DASYS	1.2	2.4	3962	0	-0.0013	0.001301
UKSYS				0.0028	0.001057	0.002992
SWESYS				0.004895	0.002822	0.00565
GECAM				0.00758	0.005083	0.009126
CANCAM				0.008628	0.005965	0.010489
ELVISS				0.009324	0.006551	0.011396
LASSIE				0.010143	0.00724	0.012462
OAGEN1	2.1	1.7	3962	0.027807	0.018213	0.03324
OAGEN2	2.1	1.6	3945	0.027807	0.020815	0.034734
OAPROTRLR	0.7	2.5	3983	-0.01545	-0.0026	0.015666
OASHORTSCI	3	1.1	3938	0.055613	0.033824	0.065092
OATALLSCI	3.6	0.6	3944	0.074151	0.046833	0.087703
OASCIBLS	2.5	1.5	3947	0.040165	0.023417	0.046493

Table 2. GPS and derived rectilinear coordinates for the 500 M target and control area relative to a fixed origin of latitude X0=32° 38' N and longitude Y0=106° 20' W.

Point	Lat (X0+X'')	Lon (Y0+Y'')	Elev (ft)	Y-N (km)	X-E (km)	R (km)
500MGASSVN	6.1	16.9	3955	0.151391	-0.37727	0.406509
500MSCRCVR	6	15.9	3944	0.148302	-0.35125	0.381273
500MSCTRNS	4.6	12.8	3942	0.105047	-0.27059	0.290268
500MTABLE	9.2	9.6	3943	0.24717	-0.18733	0.310138
500MTREE	6.5	15.9	3942	0.16375	-0.35125	0.387542
500MRC	4.4	20.5	3967	0.098868	-0.47094	0.481202

Table 3. GPS and rectilinear coordinates for location points at the 1 KM target area relative to a fixed origin of latitude X0=32° 38' N and longitude Y0=106° 20' W.

Point	Lat (X0+X'')	Lon (Y0+Y'')	Elev (ft)	Y-N (km)	X-E (km)	R (km)
1K3D	26	27.6	3959	0.766226	-0.65562	1.008436
1KVAN	18.5	28.7	3959	0.534504	-0.68426	0.868276
1KPROPANEM	19.9	29.8	3955	0.577759	-0.71287	0.917603
1KSHORTSCI	19.3	27.2	3969	0.559221	-0.64523	0.853844
1KTALLSCI	18.8	27.9	3953	0.543773	-0.66344	0.857815
1KCHKRBRD2	25.9	27.8	3951	0.763136	-0.66083	1.009489
1KLETR2	25.8	27.8	3955	0.760047	-0.66083	1.007156
1KGSCI01	21.2	27.3	3955	0.617924	-0.64783	0.895272
1KTALLMET	18	29.3	3962	0.519056	-0.69987	0.871342
1KTSOINIC	19.5	28.2	3960	0.565401	-0.67125	0.877639

Table 4. GPS and rectilinear coordinates for locations within the 2 KM target area relative to a fixed origin of latitude X0=32° 38' N and longitude Y0=106° 20' W.

Point	Lat (X0+X'')	Lon (Y0+Y'')	Elev (ft)	Y-N (km)	X-E (km)	R (km)
2K3DTGT	49.9	51.9	3943	1.504645	-1.28774	1.98046
2K50FTTBRD	49.8	52.2	3937	1.501556	-1.29554	1.983203
2KCHKRBRD	49.8	51.6	3936	1.501556	-1.27993	1.973042
2KGSCIN01	49	52.9	3968	1.476839	-1.31375	1.976614
2KGSCIN02	48.5	53.6	3958	1.461391	-1.33197	1.977321
2KLOWSCINT	49.1	54.8	3961	1.479928	-1.36318	2.012077
2KSCAFFOLD	50.5	53.1	4025	1.523183	-1.31895	2.014874
2KSHORTSCI	48.7	53.6	3959	1.46757	-1.33197	1.981892
2KTALLSCI	49	52.9	3971	1.476839	-1.31375	1.976614
2KLETT2	50	51.5	3956	1.507735	-1.27733	1.976065
2KVAN	48.6	53.7	3968	1.46448	-1.33457	1.981356

Table 5. Description key for site location labels.

Label	Description
USSYS	SWIR system (U.S.-NVEOL)
DASYS	Visible band system (Denmark)
UKSYS	SWIR system (U.K.)
SWESYS	Visible band system (Sweden)
GECAM	CCD camera system (Germany)
CANCAM	CCD camera system (Canada)
ELVISS	ELVISS SAR system (Canada)
LASSIE	LASSIE imaging system (Canada)
OAGEN1	Portable 120 VAC diesel power generator #1
OAGEN2	Portable 120 VAC diesel power generator #2
OAPROTRLR	Propagation equipment trailer (hitch area)
OASHORTSCI	ARL optical scintillometer (2 m short scaffold)
OATALLSCI	ARL optical scintillometer (4 m tall scaffold)
OASCIBLS	Scintec optical scintillometer transmitter (Germany)
500MGASSVN	GASS van entry door
500MSCRCVR	Short path optical scintillometer receiver (Canada)
500MSCTRNS	Short path optical scintillometer transmitter (Canada)
500MTABLE	500 m painted plate target table (Canada)
500MTREE	500 m met instrument ensemble (Canada)
500MRC	Radio communication station (front entrance)
1K3D	1 KM site position for 3-D target (U.S.)
1KVAN	1 KM site location of ARL instrument van (U.S.)
1KPROPANEM	Propeller anemometer location (U.S.)
1KSHORTSCI	1 KM site 2 m AGL ARL scintillometer (U.S.)
1KTALLSCI	1 KM site 4 m AGL ARL scintillometer (U.S.)
1KCHKRBRD2	1 KM site location for checkerboard target "eye chart" (U.S.)
1KLETT2	1 KM site location for billboard letter target (Canada)
1KGSCI01	1 KM site Scintec optical scintillometer receiver (Germany)
1KTALLMET	1 KM site 8 m ARL tall met tower (U.S.)
1KTSONIC	1 KM site sonic anemometer location (U.S.)
2K3DTGT	2 KM site position for 3-D target (U.S.)
2K50FTTBRD	2 KM site position for 50 m system registration target (U.S.)

Table 5. Description key for site location labels (continued).

Label	Description
2KCHKRBRD	2 KM site location for checkerboard target “eye chart” (U.S.)
2KGSCIN01	2 KM site Scintec optical scintillometer receiver #1 (Germany)
2KGSCIN02	2 KM site Scintec optical scintillometer receiver #2 (Germany)
2KLOWSCINT	HELSTF scintillometer location (2 m) (U.S.)
2KSCAFFOLD	Front of scaffold atop berm behind 2 KM target area
2KSHORTSCI	2 KM site 2 m AGL ARL scintillometer (U.S.)
2KTALLSCI	2 KM site 4 m AGL ARL scintillometer (U.S.)
2KLETT2	2 KM site location for billboard letter target (Canada)
2KVAN	2 KM site location of HELSTF instrument van (U.S.)

## 2.6 Test Day Planning

Our test schedule was planned in advance based primarily on two issues. First, several other competing missions occurred during the time of the RTG-40 test. Second, the number of conflicting missions was increased by the Missile Flight Safety plan requirement that airspace be cleared up to 10,000 ft. Because of our low priority, this stricture effectively kept us from operating anytime there were aircraft between the surface and 10,000 ft. This left us with only four windows of operations during the test week and two short windows during the preparation week.

Fortunately, the two short windows during the setup week did allow us to determine some critical information regarding system performance. First, we knew that a problem could likely exist for the Swedish system because of its power levels. To avoid the possibility that energy could exit the HELSTF range, the Swedish system was aligned so that the illumination beacon spot fell on a point below the centerline of the observation system. The illumination pulses would thus not overshoot the target berm at 2 km. Second, the U.K. system was found to have a faulty imager during one of the short window periods. Through some determined tinkering over the weekend, the U.K. team was able to repair their sensor and return from the weekend break with a fully functioning system.

Supporting us in establishing lasing times was Mark Simmons of the HELSTF group. He and Gary Wilson of the HELSTF safety group coordinated with WSMR range scheduling to establish four lasing periods during the test week. These were 0600–1000 Monday 14 November, 0500–0900 Wednesday 16 November, and 1600–1900 that evening, and 1700–2000 on Thursday 17 November. Although these were the only lasing periods, additional passive measurements were made via the scintillometer and sonic anemometer devices, the Canadian met instrument mast, and the high speed cameras of Canada and Germany when lasing operations were not being conducted.

The conduct of lasing operation days was fairly straightforward. The period usually began approximately an hour and a half prior to lasing with personnel arriving at the outer gate of

HELSTF as an assembly point. Once personnel had arrived, escorts were assigned to foreign visitors and a caravan of vehicles was formed up to travel inside the HELSTF gate to the downrange test area. Once at the area active systems crews would begin startup procedures on their systems. These procedures usually took no more than half an hour. Also, once on site the Canadian group would send a party to the 500 m area to activate their met data acquisition systems.

Usually the ARL met technician crew of Jimmy Yarbrough and Ed Vidal were onsite prior to the rest of the group to download data, restart the data acquisition system if necessary, and to check logistical items such as the condition of the diesel electrical generators. Approximately 40 minutes prior to commencement of lasing operations the HELSTF safety crew would arrive to begin coordinating with WSMR range control. At 30 minutes prior to lasing the downrange area to the northwest of the laser line in the OA would be cleared, except for the ARL communications group of Gail Vaucher and Lou Lucas at a trailer out of the propagation area behind the 500 m downrange building. From this location, their FRS radios could reach any point of the downrange area.

Once the range had been cleared and clearance was received from WSMR range, the laser line became active. Only personnel properly goggled for the type of laser being fired at the time were permitted on the laser line. Since there were essentially three different wavebands of lasers (visible (532 nm), NIR (810 and 860 nm), and SWIR (1570 nm)), the typical procedure was to test similar wavelength devices in succession. Hence, the Danish and Swedish visible systems were typically tested back-to-back, as were the two Canadian NIR systems. At the SWIR waveband, unfortunately, because the NVESD system developed difficulties, the U.K. system was tested separately. Once each system had been tested against each target, the procedure was repeated with as many repetitions as possible. Typically the testing of a given system required 8–10 minutes to sense all available targets. In a four hour time window, the result was approximately 4 to 5 complete sets for each sensor. Safety concerns regarding control of multiple lasers simultaneously prevented us from lasing with more than one device at a time. It would also have been impossible to goggle properly for two different wavelengths at once since the goggles available could only shield for one wavelength band at a time.

Some experience was required to learn to use time wisely during the testing periods. Tuesday of the setup week was our first experience with laser operations and much time was lost organizing the activities involved. We managed to adjust the Swedish and Danish systems, but the Canadian systems could not operate during daylight due to low laser power. We also ran out of time to check on the NVESD system.

On Wednesday (10 November) we had our second chance to test the systems and were somewhat more successful. It was during this testing that the U.K. staff recognized their instrument was malfunctioning. The NVESD system also appeared to come on line, but

apparently the laser overheated. It was believed at the time that it would operate on Monday morning once the unit had cooled.

On Monday (14 November) we began the first set of measurements. As we were starting prior to dawn, the Canadians were permitted to gain extra time prior to dawn to test their systems. Then, after sunrise, the other systems were alternated: the Danish, Swedish, and U.K. systems. But because the NVESD system was not coming up, an attempt was made to block out extra time so that this system could be tested to see if it could come up. Even with the extra time, it became clear the unit's imager was not working properly. Eventually the NVESD unit was shipped out on Tuesday afternoon.

On Wednesday morning the NVESD group refocused their efforts on setting up their downrange camera. This instrument is designed to set up at approximately 30–80 m from a target in the LOS of an illuminating laser system so that a sensor on the back of the camera can detect a laser pulse arriving. The camera then triggers the system aperture to open briefly so that an image of the illumination pulse on the target can be imaged. Richard Espinola of NVESD was sent downrange along with Jimmy Yarbrough of ARL and Bob Street of HELSTF safety to operate this camera during the experiments. After some discussion regarding safety issues, it was agreed that these individuals could remain downrange as long as they were properly goggled for the laser system in operation. After some further adjustments, the downrange camera was brought on line and three 30-second sequences of illumination pulses were captured, as provided by the U.K. BIL system. Simultaneously the U.K. system was detecting the returned images of the same scenes.

## **2.7 Post-Test Activities**

At the conclusion of the test, several matters of consequence still needed to be accomplished. First, the ARL crew cleared equipment from the site. Second, equipment needed to be shipped back to Europe, which caused some problems, depending on the shipper. Third, the data needed to be extracted from the Structured Query Language (SQL) database and hourly files produced for purposes of distribution to the NATO RTG-40 group. Fourth, the analysis discussed in the next section was begun. This involved both software development and access to the data. Fifth, the scintillometers were recalibrated. This last step is described in the appendix.

---

## **3. Initial ARL Data Analysis**

---

The ARL met data has been analyzed to characterize the atmospheric conditions under which the optical measurements were collected, as well as the varying met conditions present during the entire experimental period. Several statistical and derived-parameter calculations of the data were made, focusing initially on the mean parameters, and using data taken by the sonic

anemometers and other sensors. Of primary interest in the initial analysis were the means of temperature, wind,  $C_n^2$ , and solar radiation. Subsequently, the computed fluxes of sensible heat and momentum were considered. The calculation of  $C_n^2$  directly from the sonic anemometers data and the determination of the inner scale of turbulence from these data was then considered. An ancillary study was also performed after the RTG-40 test to determine means of extracting better relative temperatures from the temperature sensors on the sonic anemometers.

### **3.1 Data Acquisition**

The data collection for the ARL met sensors was undertaken using a series of acquisition routines based on Java-spaces developed by Edward Vidal of ARL/WSMR. The software/hardware data acquisition architecture for the sonic anemometers was implemented differently than that which was used for the scintillometers and radiation sensor. The former devices generate ASCII signals and may be transmitted on either RS-232 or RS-485, serial data lines. These data were carried from the sensor on RS-485 lines to the Sensor Interface Module (SIM) converted to transistor-transistor logic (TTL) and fed to an RCM 3000 microprocessor. The data are then directly ingested via 802.3 Ethernet into one or more laptop personal computers (PCs). The data rate for the sonics was set to 20 Hz. The data from the Lockheed scintillometers and the Kipp and Zonen radiometer was first fed to a Rabbit RCM 3400 Prototyping Board mounting a Rabbit RCM 3400 Rabbitcore microprocessor in order to first digitize the analog signals, then ingested via 802.3 Ethernet into a laptop PC. The data rates for the scintillometers were set at 40 samples per minute. The same data rate was chosen for the radiometer, since the incident sunlight was not expected to vary significantly on the order of a second. The sampling rate for the scintillometers is slow because the processing hardware internal to the devices is low pass filtered. The Rabbit then time stamped each record of the data and output it, via Ethernet 803.2 to the archiving PC.

The software used to archive the data was developed over several years and included several phases. The primary storage for the data was within an SQL database. To merge data into that database, two archiving PCs were used. The initial ingest into the archival system was via input “workers” within the Java-based system. These workers would read the data input from the serial input lines and input the data into the Java “space.” Once in the space, the data would await a second worker that would send the data into the SQL database. The database was located on one of the computers. This machine ingested data from one of the sonics and all of the scintillometer and radiometer data. The other machine ingested data from the remaining sonics and transferred this data into the main archiving PC.

Because of the volume of data being archived to the database, the data sets needed to be periodically dumped to other storage media. This process took the better part of an hour, during which the data acquisition process had to be temporarily halted. This created gaps in the data sets of roughly one hour intervals on the 10<sup>th</sup> and 15<sup>th</sup> of November.



### 3.2 Computing Mean and Second Order Statistics

The first stage of the data analysis was to develop plots of mean temperatures and winds from the sonic anemometer data, as well as mean scintillometer output and radiation data. From these data a more comprehensive and accurate picture of the measurement period can be appreciated. For the most part, the period of measurement was not characterized by extremes of weather events. The only critical events occurred when high winds were briefly present. Otherwise, the skies were relatively clear (some high clouds), and the winds were fairly moderate. Mean plots of weather parameters derived from observations were thus somewhat representative of the state of the atmosphere over reasonably large spans of space and time. These longer-period norms were used as starting points for a second phase in the analysis where higher order statistics are described.

A Hanning window weighting function was employed to evaluate mean effects. Under this weighting approach, a Full Width at Half Maximum (FWHM) of 15 minutes was used to generate 15 minute averaged effects. The results of these calculations were then output every 5 minutes. These averages represented a compromise between the 30 minute averages recommended in personal communications with J. Churnside of NOAA's Wave Propagation Laboratory, Boulder, CO, some years ago, and the variability of atmospheric conditions present. Of course, for conditions that are static or linearly trending, the distinction is irrelevant, since the same mean value will result regardless of the averaging period. For fluctuating atmospheric conditions, driven by such factors as variable cloud cover, nocturnal stability conditions, or rapidly evolving conditions at the neutral event, shorter time averages are recommended. A compromise between the 30 minute average and these shorter-term periods is required because very short averaging intervals will tend to reflect higher frequency (e.g., turbulent) fluctuations rather than the evolution of the mean.

The Hanning window (cf. Ludemann, 1986) is expressed by

$$W_H(x) = [1 - \cos(2\pi x / X)] / X, \quad (1)$$

where  $x$  ranges from 0 to  $X$ . Numerically, the weighting function is evaluated by computing the numerator of the weighting function at each time in the period, summing the coefficients over the complete integration interval, and subsequently dividing each weight element by the summation. The new sum of weight terms will then equal 1.0. Use of this approach yields an equivalent 15 minute average, but has smoothly truncated ends. It thus is also directly comparable to a similarly weighted Fast Fourier Transform (FFT) analysis, where the apodizing window function is used to minimize aliasing.

The window-weighted winds at each tower level for the sonic anemometer data at the ARL 1 km site tower are plotted for each day of the measurement period starting on November 9<sup>th</sup> through the 18<sup>th</sup> in figures 13 through 22.

Note the varying scale of the plots, depending on the maximum wind speed for the given day.

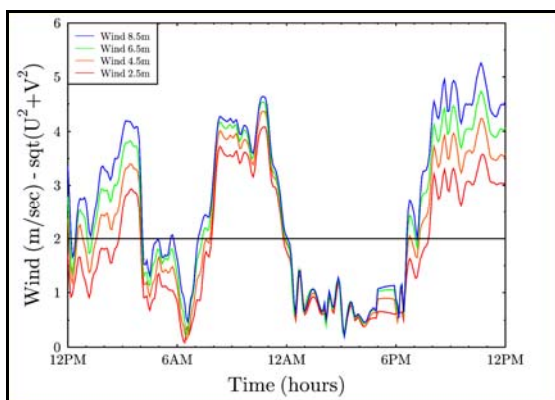


(Figure 13-November 9<sup>th</sup>)

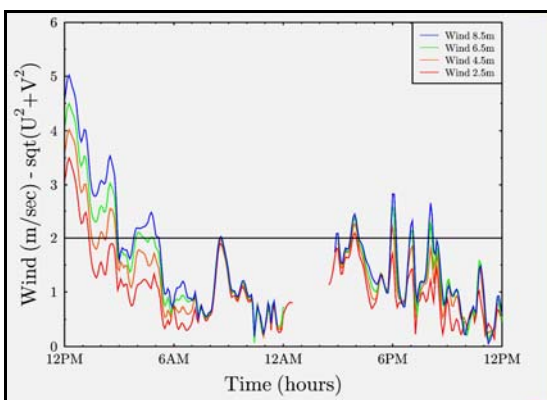


(Figure 14-November 10<sup>th</sup>)

Figures 13 and 14. Fifteen-minute mean horizontal wind speeds during November 9<sup>th</sup> and 10<sup>th</sup> for 2.5, 4.5, 6.5, 8.5 m sonic anemometer levels.

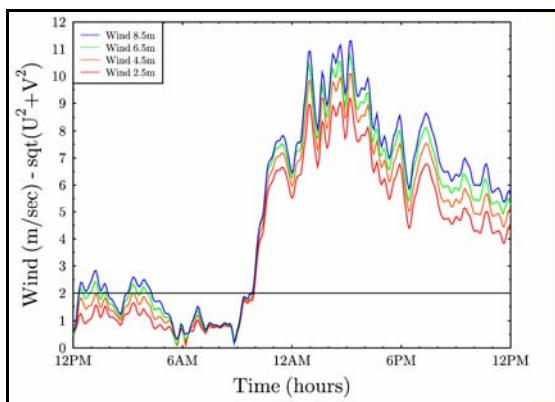


(Figure 15-November 11<sup>th</sup>)

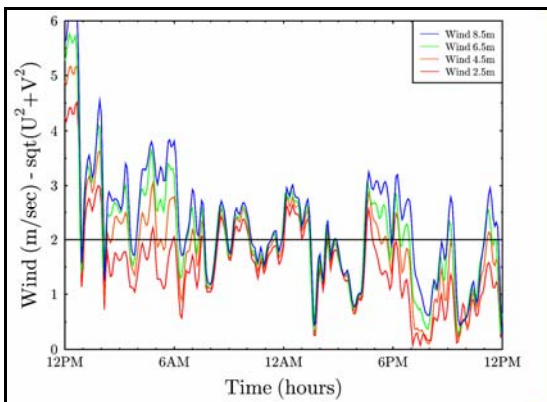


(Figure 16-November 12<sup>th</sup>)

Figures 15 and 16. Fifteen-minute mean horizontal wind speeds during November 11<sup>th</sup> and 12<sup>th</sup> for 2.5, 4.5, 6.5, 8.5 m sonic anemometer levels.

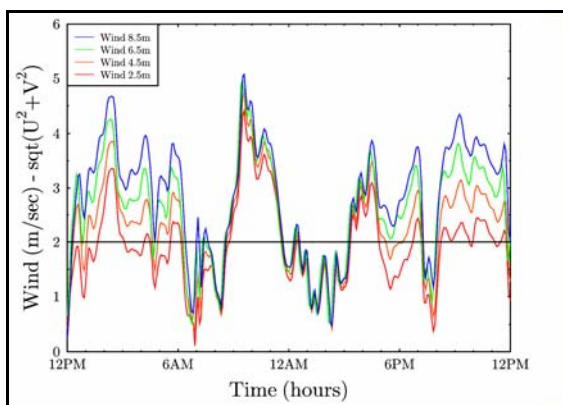


(Figure 17-November 13<sup>th</sup>)

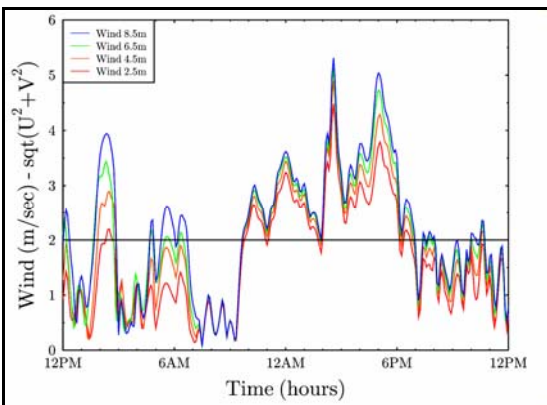


(Figure 18-November 14<sup>th</sup>)

Figures 17 and 18. Fifteen-minute mean horizontal wind speeds during November 13<sup>th</sup> and 14<sup>th</sup> for 2.5, 4.5, 6.5, 8.5 m sonic anemometer levels.

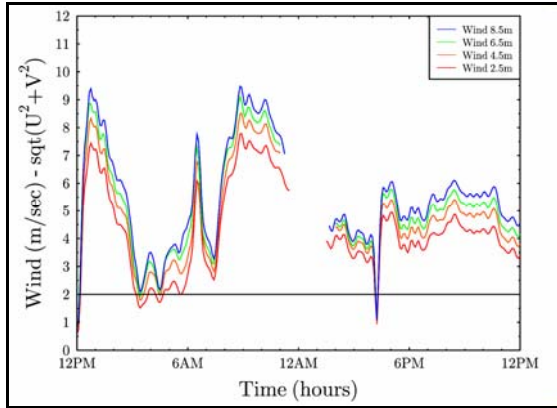


(Figure 19-November 15<sup>th</sup>)

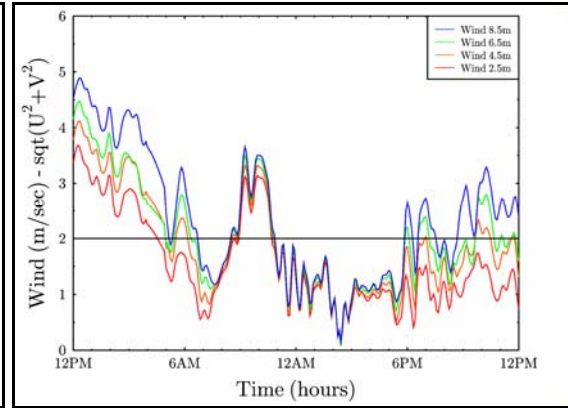


(Figure 20-November 16<sup>th</sup>)

Figures 19 and 20. Fifteen-minute mean horizontal wind speeds during November 15<sup>th</sup> and 16<sup>th</sup> for 2.5, 4.5, 6.5, 8.5 m sonic anemometer levels.

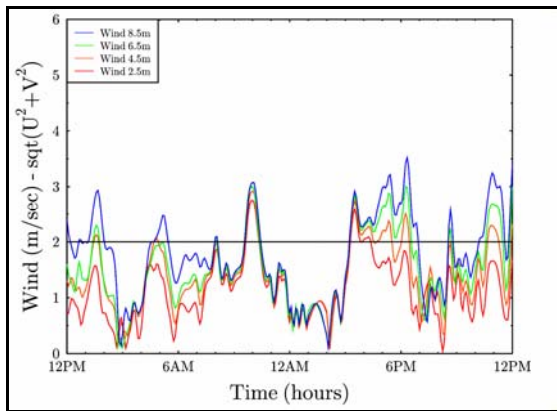


(Figure 21-November 17<sup>th</sup>)

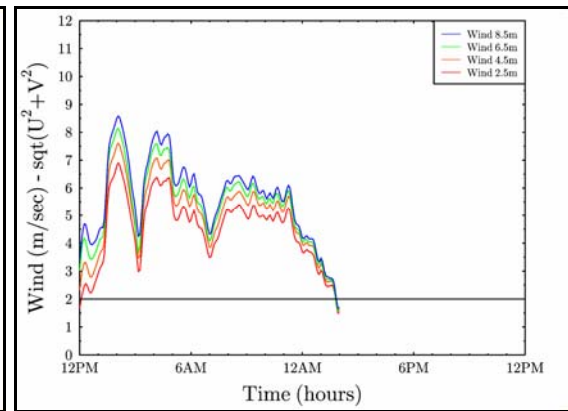


(Figure 22-November 18<sup>th</sup>)

Figures 21 and 22. Fifteen-minute mean horizontal wind speeds during November 17<sup>th</sup> and 18<sup>th</sup> for 2.5, 4.5, 6.5, 8.5 m sonic anemometer levels.

A qualitative assessment of these measurements revealed two anomalies in the 6.5 m (green line) sonic data. These effects appeared intermittently, later in the experimental period. The first of these phenomena is manifested when the wind speeds recorded by the 6.5 m sensor appear to fall below the 4.5 m wind values at times, particularly in the early morning hours of the 16<sup>th</sup> (figure 20) and 17<sup>th</sup> (figure 21). Less obvious from the plots is the second anomaly, which is an apparent timing issue. Fluctuations in the 6.5 m data from the 13<sup>th</sup> and 14<sup>th</sup> seem to be temporally advanced by about 5 minutes ahead of locally similar variations at the other three sensor levels. The cause of this time advance is unknown, but calls into question the use of the 6.5 m data on several days of the data collection period. The determination of which of the 6.5 m sonic data to reject can better be determined at a later point by a momentum flux intercomparison among the different sensor levels. Good consistency exists for the remaining 2.5 m, 4.5 m, and 8.5 m wind data throughout the measurement period.

### 3.3 Temperature Corrections

A second parameter data set analyzed using the 15 minute averaged weighting scheme was the sonic temperature data. The RM Young sonic temperatures exhibit systematic biases between their reported temperatures and the actual temperature, an offset that is different from sensor to sensor. Measured values for this bias for a given sensor appear to be constant over the test period. Thus, the temperatures measured at the different levels of the tower can be adjusted relative to one another to produce a model of the relative vertical temperature structure, provided that the sensors all experience the same absolute temperature. This condition would correspond to one of the neutral events sensed during the experiment (as suggested by Cheryl Klipp, ARL, personal communication). In particular, the best neutral events would be accompanied by high winds. Such conditions occurred during the neutral events on the evenings of November 11<sup>th</sup> and 15<sup>th</sup>.

Based on analysis of these data sets, the 4.5 m, 6.5 m, and 8.5 m tower temperatures were adjusted to the same relative temperature as the 2.5 m sensor by subtracting amounts 1.70, 0.67, and 0.68 °C, respectively, from data from the 4.5 m, 6.5 m, and 8.5 m sensors.

On November 11th, the evening neutral event occurred between minutes 970 (16:10) and 980. The offsets of the 4.5 m, 6.5 m, and 8.5 m sensors from the 2.5 m sensor were as follows:

	4.5 m	6.5 m	8.5 m
970	1.823	0.652	0.668
975	1.827	0.678	0.682
980	1.833	0.685	0.697

While the transition for the 2.5 m and 4.5 m sensors was approximately at the same time of 970 minutes, the transition times for the 6.5 m and 8.5 m sensors were slightly delayed due to the upward progression of the neutral temperature profile after the surface heat flux crossover time. Thus, more than one time had to be considered at these higher levels.

On November 15th, the neutral event occurred between minutes 990 (16:30) and 1000:

	4.5 m	6.5 m	8.5 m
990	1.670	0.604	0.624
995	1.682	0.633	0.656
1000	1.697	0.665	0.692

Two issues are of note here. First, the 6.5 m and 8.5 m temperature offsets appear consistent, while the 4.5 m offset is somewhat inconsistent. The selection of an offset of 1.70 °C was ultimately based more on art than science, a trial and error choice based on the data from the evening of the 15<sup>th</sup> after sunset. The “art” in this procedure was to place the 4.5 m data track between the 2.5 m and the 6.5 m temperature tracks. The offset selected produced this result. The choice also worked well on the other days. Plots of these temperature tracks are shown in figures 23 through 32.

Interestingly, the 6.5 m sensor displays marked deviations from the expected temperature vertical profile behavior at about the same times as the aforementioned wind speed anomalies (see, in particular, figures 30 and 31). Fortunately, periods where the 6.5 m sensor appears to be producing inappropriate results are not those associated with the imaging sensor data collection periods of the RTG-40 testing.

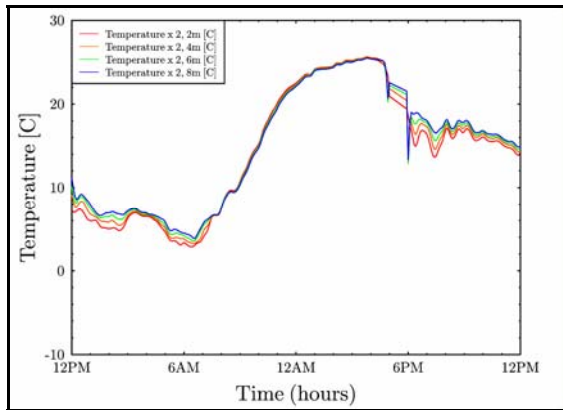


(Figure 23-November 9<sup>th</sup>)

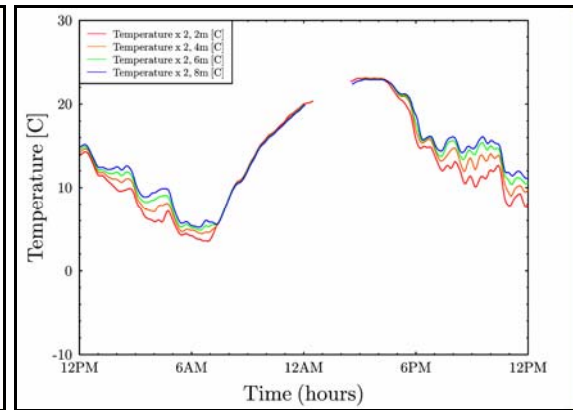


(Figure 24-November 10<sup>th</sup>)

Figures 23 and 24. Fifteen-minute mean temperature plots for November 9<sup>th</sup> and 10<sup>th</sup> for 2.5, 4.5, 6.5, 8.5 m sonic anemometer levels.

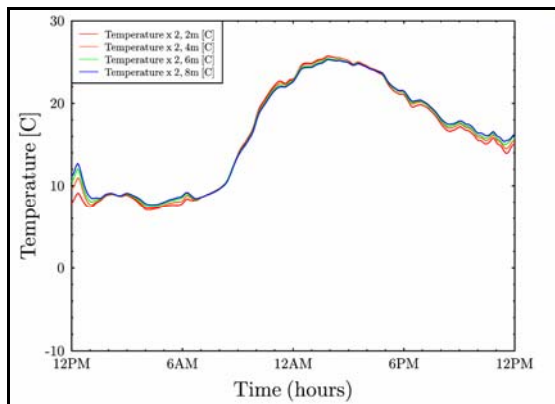


(Figure 25-November 11<sup>th</sup>)

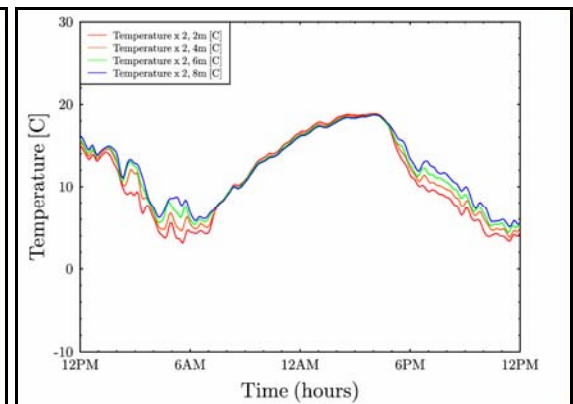


(Figure 26-November 12<sup>th</sup>)

Figures 25 and 26. Fifteen-minute mean temperature plots for November 11<sup>th</sup> and 12<sup>th</sup> for 2.5, 4.5, 6.5, 8.5 m sonic anemometer levels.

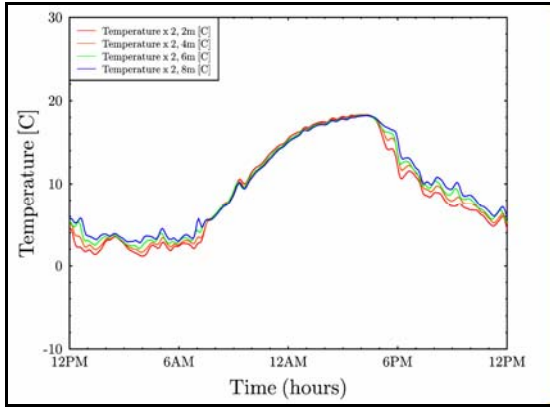


(Figure 27-November 13<sup>th</sup>)

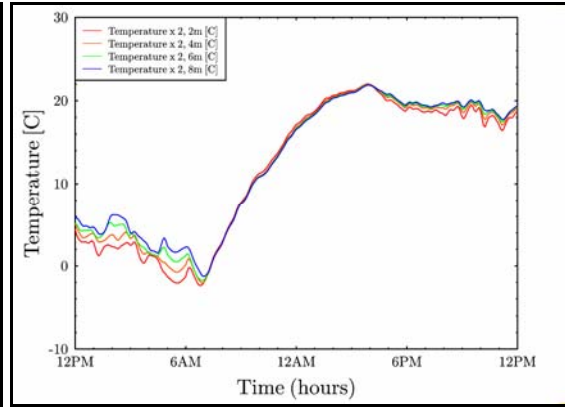


(Figure 28-November 14<sup>th</sup>)

Figures 27 and 28. Fifteen-minute mean temperature plots for November 13<sup>th</sup> and 14<sup>th</sup> for 2.5, 4.5, 6.5, 8.5 m sonic anemometer levels.

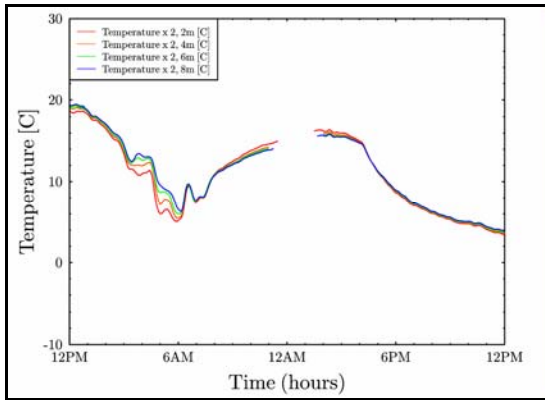


(Figure 29-November 15<sup>th</sup>)

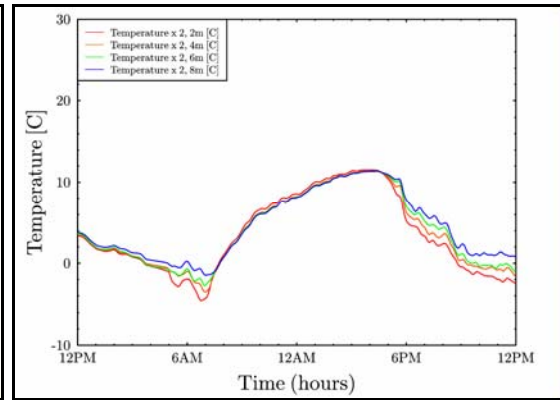


(Figure 30-November 16<sup>th</sup>)

Figures 29 and 30. Fifteen-minute mean temperature plots for November 15<sup>th</sup> and 16<sup>th</sup> for 2.5, 4.5, 6.5, 8.5 m sonic anemometer levels.

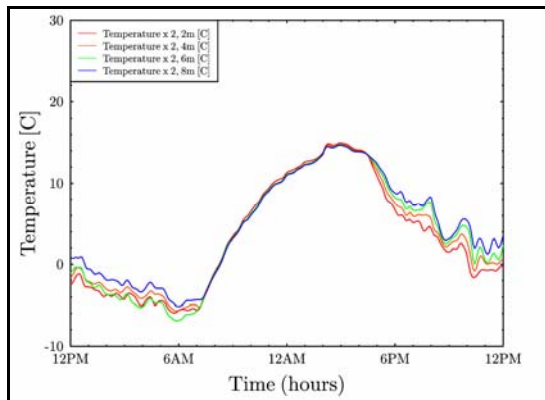


(Figure 31-November 17<sup>th</sup>)

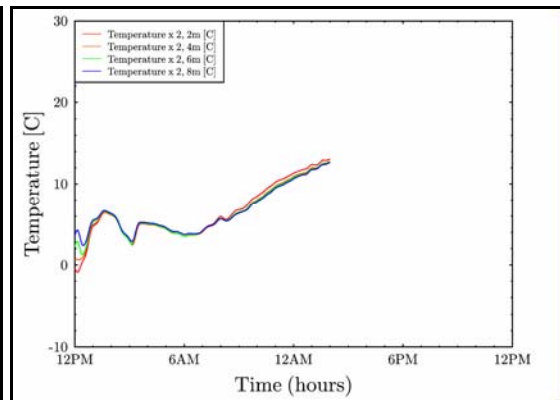


(Figure 32-November 18<sup>th</sup>)

Figures 31 and 32. Fifteen-minute mean temperature plots for November 17<sup>th</sup> and 18<sup>th</sup> for 2.5, 4.5, 6.5, 8.5 m sonic anemometer levels.

### 3.4 Turbulence

To conclude our discussion of the first order data, we plot the diurnal turbulence strength in figures 33 through 42. Four scintillometers were used, but only two of these were operational most of the time, as is evident in the plots. The two southern lasers were only operational during a minority of the time, due to limited availability of both fuel for the diesel generators and support personnel at the OA. The scintillometers at the northern end of the test area were on hard (permanent) power, and thus only show downtimes due to data archival or system maintenance activities. The plots show all available data.

One of the scintillometers apparently had difficulties. The blue line indicating the turbulence level at 4 m from 1 to 2 km does not appear to capture the full variation seen by the 2 m sensor (red line), particularly at times of low turbulence near neutral events. Unfortunately, this behavior was not detected during the experiment itself. The cause of this phenomenon is difficult to determine from the mean data, which only shows low frequency trends. Because the problem is especially evident at low turbulence periods, it is possible that system noise (either optical or electronic) could have been a factor. This and other possibilities may be examined at a later point with the high frequency (instantaneous) data.

When they are available, the two southern scintillometers appear to capture the same neutral event features as the 2 m northern sensor. Further analysis of the scintillometer data is expected, but is limited to the mean trends in this document. The figures also include estimates of the  $C_n^2$  based on the spectral analysis of the 2.5 m sonic anemometer data discussed further in section 3.3.

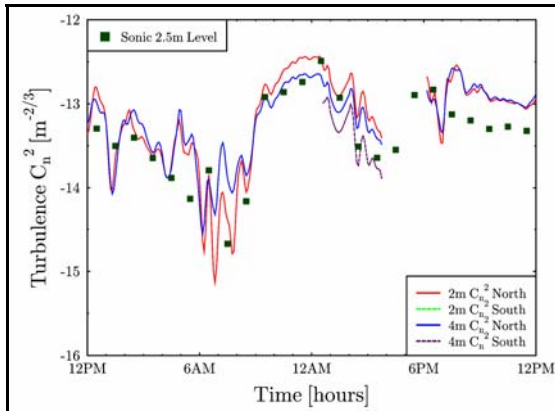


(Figure 33-November 9<sup>th</sup>)

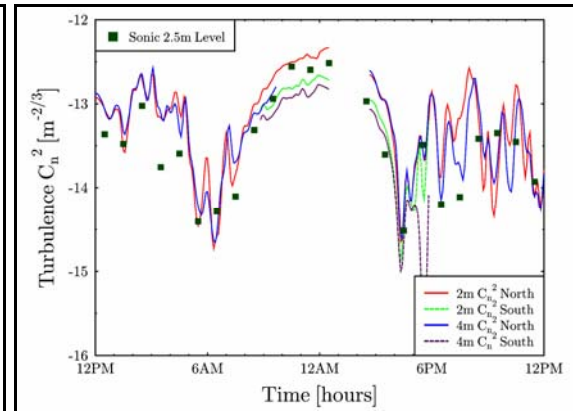


(Figure 34-November 10<sup>th</sup>)

Figures 33 and 34. Fifteen-minute mean turbulence plots for November 9<sup>th</sup> and 10<sup>th</sup> for 4 scintillometers.



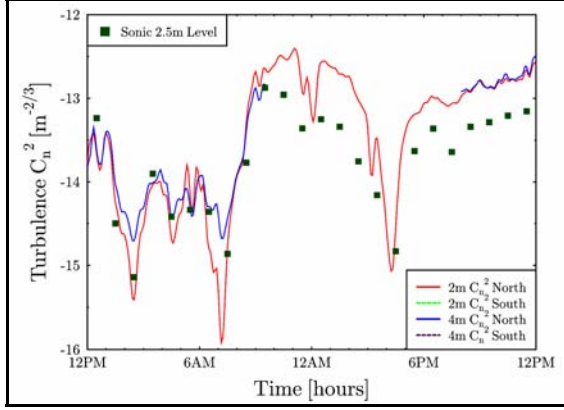


(Figure 35-November 11<sup>th</sup>)

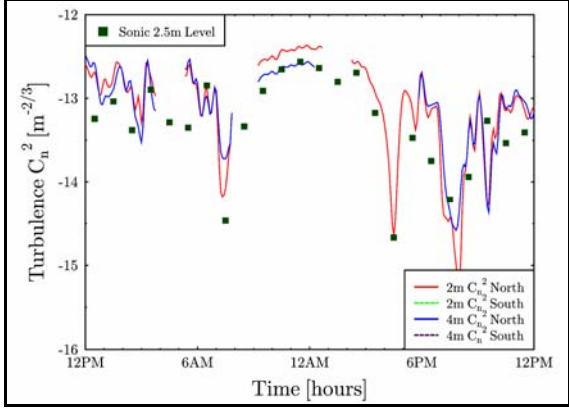


(Figure 36-November 12<sup>th</sup>)

Figures 35 and 36. Fifteen-minute mean turbulence plots for November 11th and 12th for 4 scintillometers.

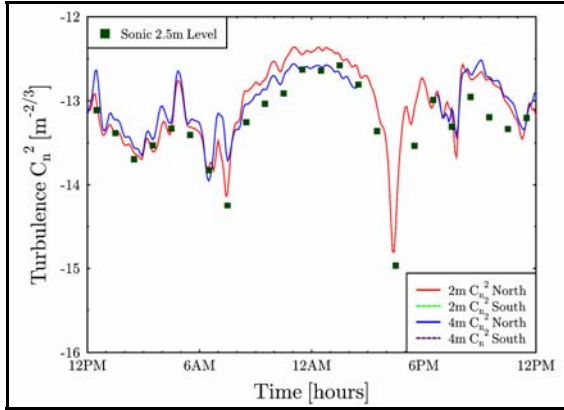


(Figure 37-November 13<sup>th</sup>)

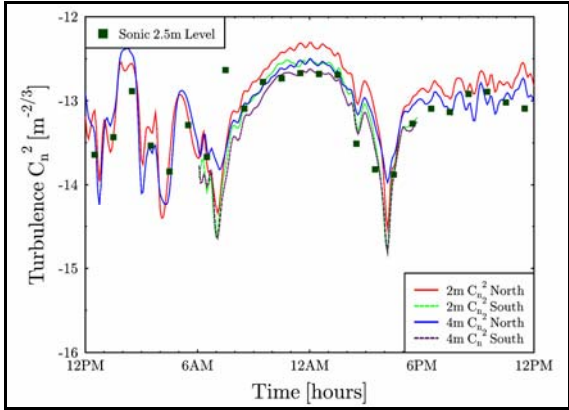


(Figure 38-November 14<sup>th</sup>)

Figures 37 and 38. Fifteen-minute mean turbulence plots for November 13th and 14th for 4 scintillometers.

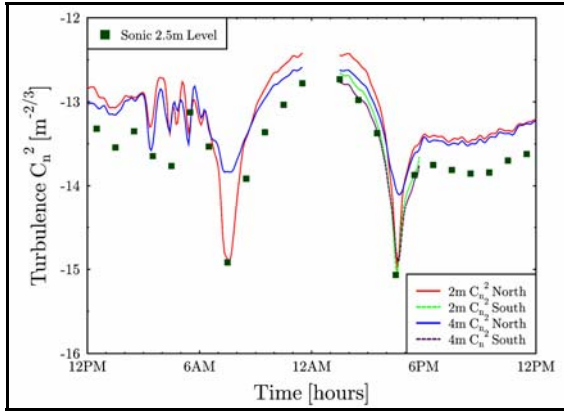


(Figure 39-November 15<sup>th</sup>)

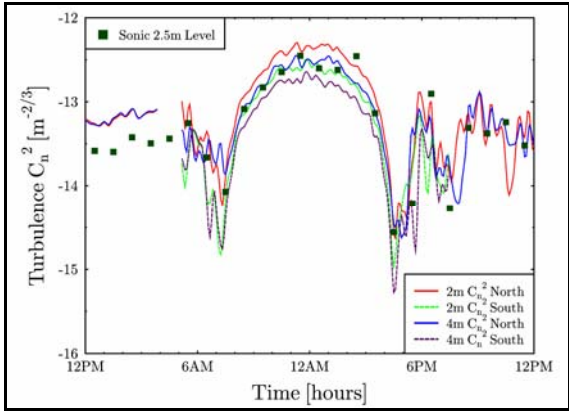


(Figure 40-November 16<sup>th</sup>)

Figures 39 and 40. Fifteen-minute mean turbulence plots for November 15th and 16th for 4 scintillometers.



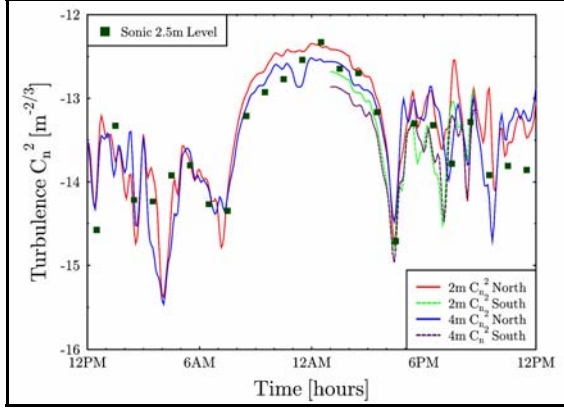


(Figure 41-November 17<sup>th</sup>)

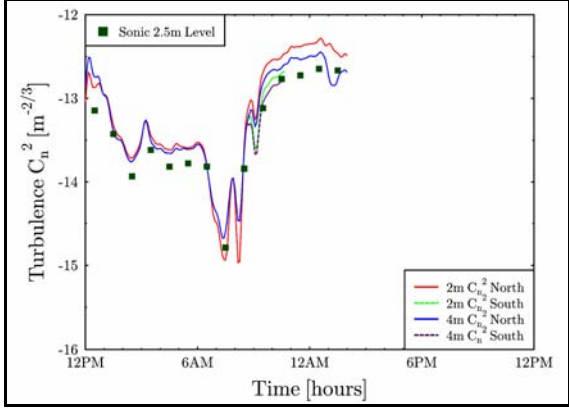


(Figure 42-November 18<sup>th</sup>)

Figures 41 and 42. Fifteen-minute mean turbulence plots for November 17th and 18th for 4 scintillometers.

### 3.5 Second Order Statistics

We next consider second order statistics related to the vertical fluxes of sensible heat and momentum. We compute flux values of  $\langle w'T' \rangle$  and  $\langle u'w' \rangle$  by removal of mean trends of the wind and temperature data and evaluating mean fluctuation products weighted according to a Hanning window weighting scheme similar to that used for the mean value calculations. The procedure for removing the local mean from the data was straightforward. First, the 5-minute averaged mean wind and temperature values were used to develop a spline of these averages over the  $\frac{1}{2}$  hour interval of the weighting period. The interpolated mean values were then removed from the sonic data. The bulk of influences due to varying winds, illumination conditions, and mesoscale type effects were thus removed, leaving only the fluctuations about the mean. The analysis method used here is essentially a fixed high-pass frequency filter approach, as opposed to a putatively more versatile dynamic high-pass filtering method such as the cospectral gap technique (Vickers and Mahrt, 2003). In most cases, the 5-minute running average should be adequate to eliminate most low frequency trends from the processed data. Results from these calculations are shown in figures 43 to 52. Plots include 15-minute averaged solar radiation data scaled at  $\frac{1}{3}$  collected value for comparison with the sensible heat computed from the sonic 2.5 m data. Also plotted is a scaled momentum flux. The significance of this intercomparison is seen during a few nights where the sensible heat flux is clearly proportional to the momentum flux.

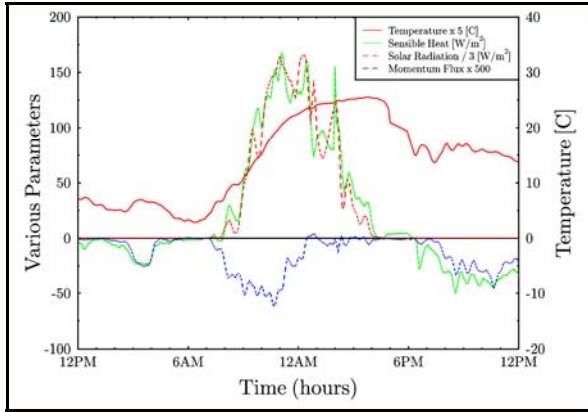


(Figure 43-November 9<sup>th</sup>)

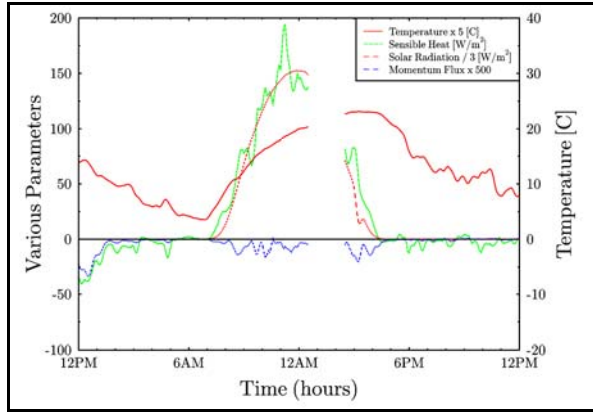


(Figure 44-November 10<sup>th</sup>)

Figures 43 and 44. Fifteen-minute mean parameter plots for November 9<sup>th</sup> and 10<sup>th</sup> for 2.5 m level.

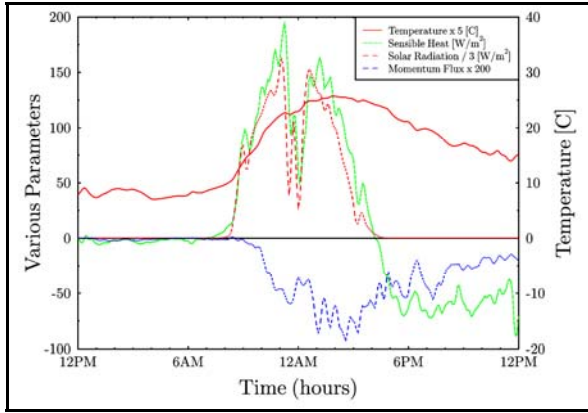


(Figure 45-November 11<sup>th</sup>)

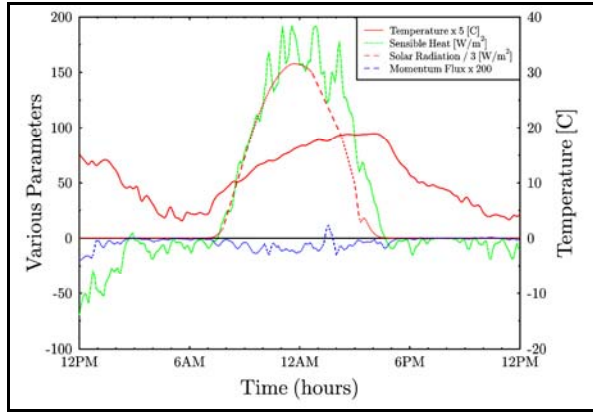


(Figure 46-November 12<sup>th</sup>)

Figures 45 and 46. Fifteen-minute mean parameter plots for November 11<sup>th</sup> and 12<sup>th</sup> for 2.5 m level.

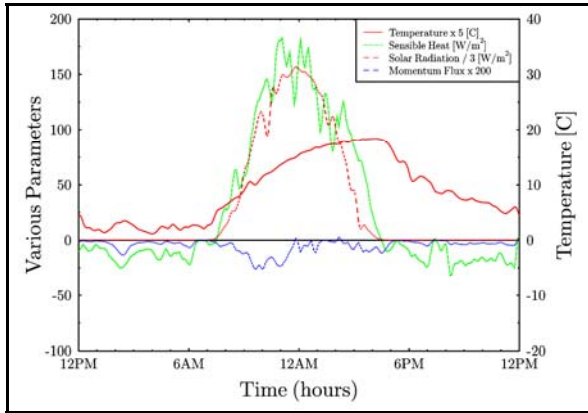


(Figure 47-November 13<sup>th</sup>)

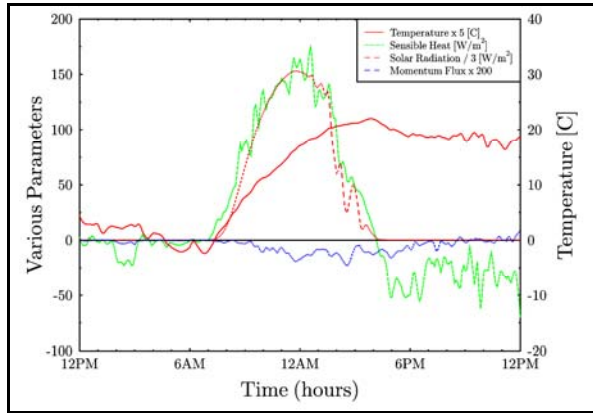


(Figure 48-November 14<sup>th</sup>)

Figures 47 and 48. Fifteen-minute mean parameter plots for November 13<sup>th</sup> and 14<sup>th</sup> for 2.5 m level.

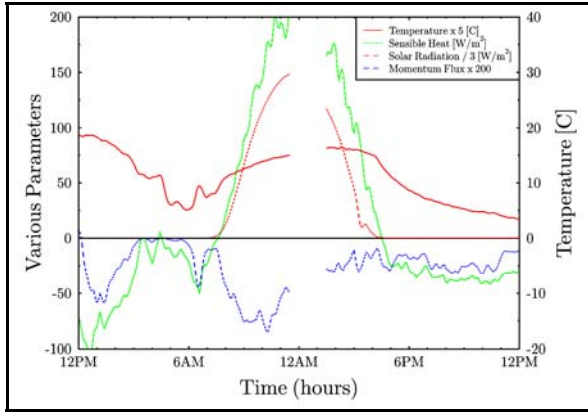


(Figure 49-November 15<sup>th</sup>)

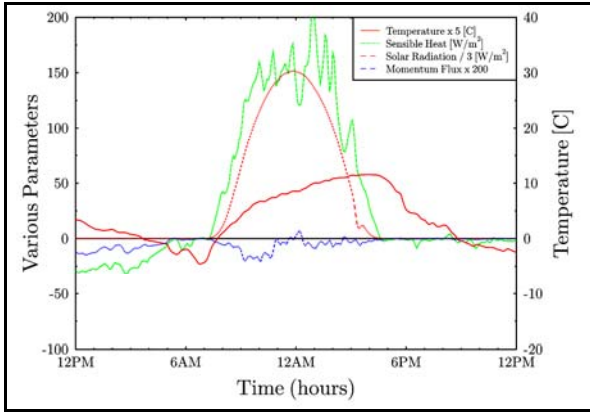


(Figure 50-November 16<sup>th</sup>)

Figures 49 and 50. Fifteen-minute mean parameter plots for November 15<sup>th</sup> and 16<sup>th</sup> for 2.5 m level.

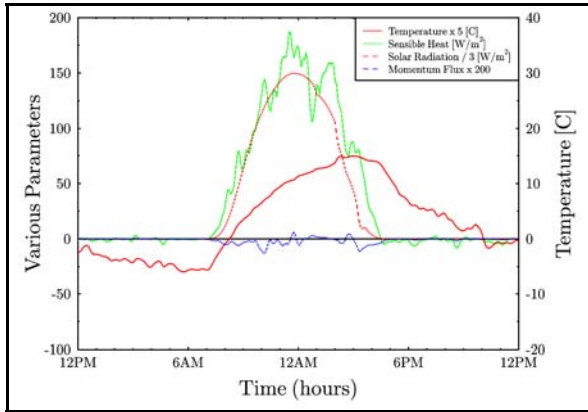


(Figure 51-November 17<sup>th</sup>)

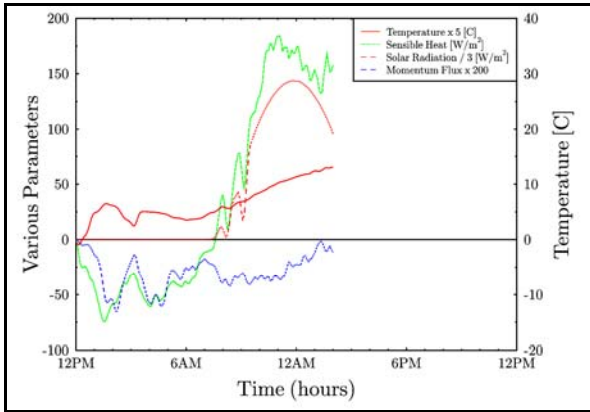


(Figure 52-November 18<sup>th</sup>)

Figures 51 and 52. Fifteen-minute mean parameter plots for November 17<sup>th</sup> and 18<sup>th</sup> for 2.5 m level.

Similar intercomparisons of parameters obtained at 4.5 m, 6.5 m, and 8.5 m were also prepared, but showed essentially the same trends, and are not shown here. Of greater interest are the simultaneous intercomparisons of either the momentum or heat fluxes obtained from the four anemometers at the different levels at the same time. These are included in figures 53 through 62 for the momentum flux intercomparisons and figures 63 through 72 for sensible heat flux.

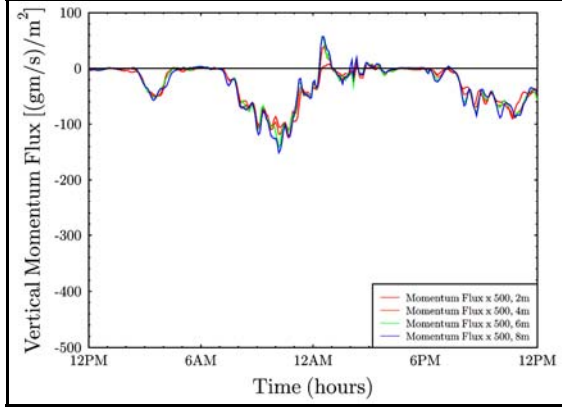


(Figure 53-November 9<sup>th</sup>)

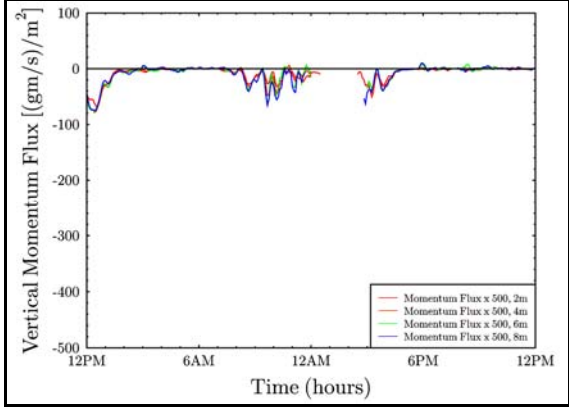


(Figure 54-November 10<sup>th</sup>)

Figures 53 and 54. Fifteen-minute mean vertical momentum fluxes for November 9<sup>th</sup> and 10<sup>th</sup> for 2.5, 4.5, 6.5, 8.5 m sonic anemometer levels.

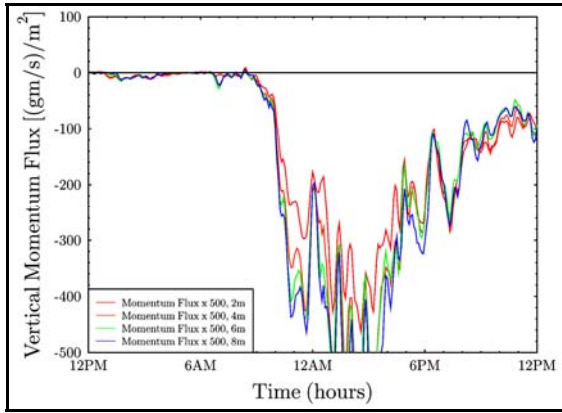


(Figure 55-November 11<sup>th</sup>)

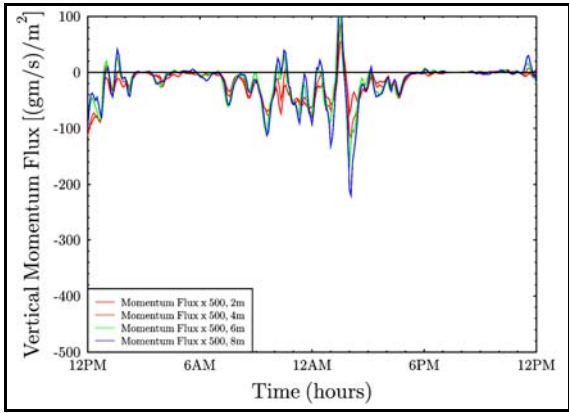


(Figure 56-November 12<sup>th</sup>)

Figures 55 and 56. Fifteen-minute mean vertical momentum fluxes for November 11<sup>th</sup> and 12<sup>th</sup> for 2.5, 4.5, 6.5, 8.5 m sonic anemometer levels.

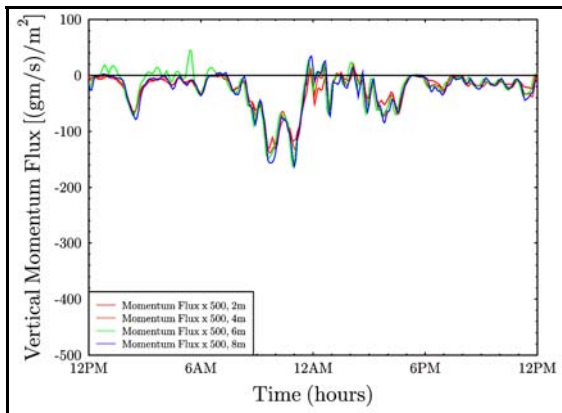


(Figure 57-November 13<sup>th</sup>)

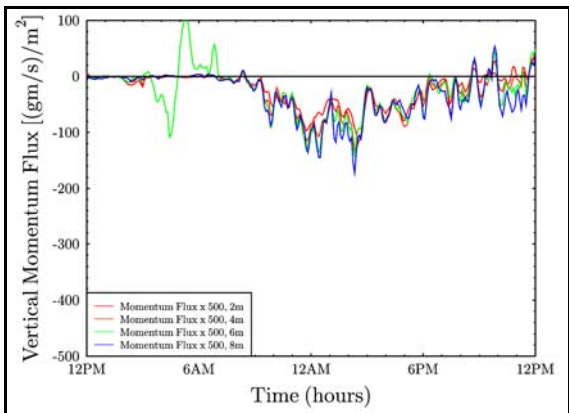


(Figure 58-November 14<sup>th</sup>)

Figures 57 and 58. Fifteen-minute mean vertical momentum fluxes for November 13<sup>th</sup> and 14<sup>th</sup> for 2.5, 4.5, 6.5, 8.5 m sonic anemometer levels.

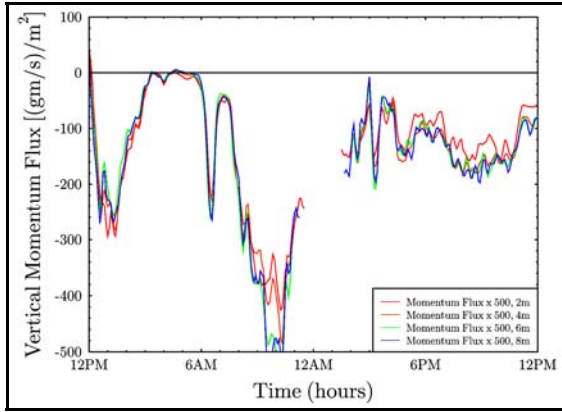


(Figure 59-November 15<sup>th</sup>)

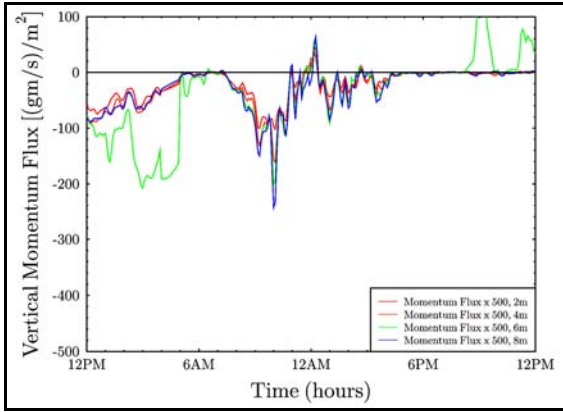


(Figure 60-November 16<sup>th</sup>)

Figures 59 and 60. Fifteen-minute mean vertical momentum fluxes for November 15<sup>th</sup> and 16<sup>th</sup> for 2.5, 4.5, 6.5, 8.5 m sonic anemometer levels.

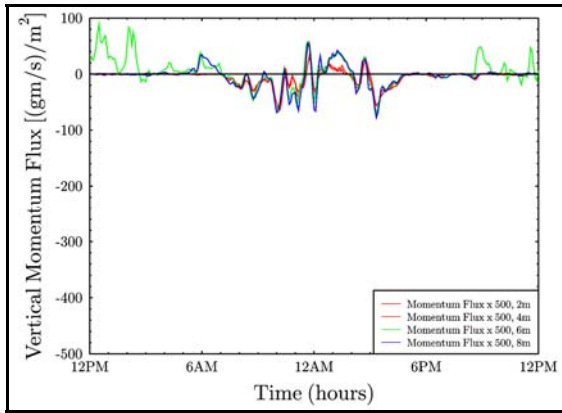


(Figure 61-November 17<sup>th</sup>)

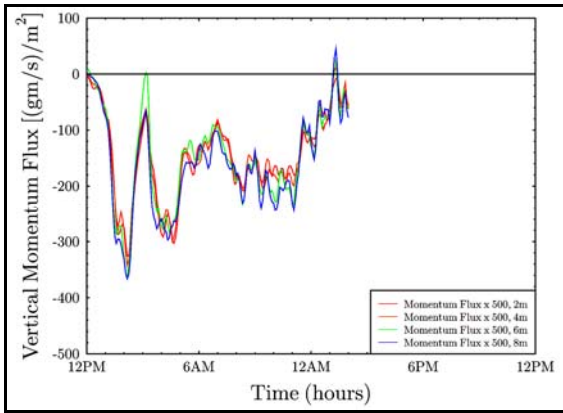


(Figure 62-November 18<sup>th</sup>)

Figures 61 and 62. Fifteen-minute mean vertical momentum fluxes for November 17<sup>th</sup> and 18<sup>th</sup> for 2.5, 4.5, 6.5, 8.5 m sonic anemometer levels.

We note as a background for our results that a major wind event occurred on the evening of November 11<sup>th</sup>, and is reflected in the data plotted in figures 3 and 55. Precautions therefore were taken to insure that all the tents were secured and plastic was wrapped over the optical instrumentation and monitors as protection from blowing dust. A similar procedure was conducted on the evening of the 14<sup>th</sup> in anticipation of a wind event to occur later that night. As seen in figures 19 and 59, the event actually occurred on the morning of the 15<sup>th</sup>, but test personnel were not permitted on site due to White Sands road blocks and where even on-site HELSTF personnel had to remain underground during testing periods.

Also of interest was the operational condition of the wind sensor at 6.5 m. It is apparent in figures 57, 58, 60, and 61, that the sensor was intermittently in error on the 13<sup>th</sup>, 14<sup>th</sup>, 16<sup>th</sup>, and 17<sup>th</sup>. The occurrence of these errors appears to be in conjunction with cold weather conditions. On the morning of the 13<sup>th</sup> the temperature first reached approximately 3 °C for an extended



period. Thereafter, on the other days listed above, the temperature was at or below this temperature. The phenomenology indicates the possibility of a loose solder joint that shrinks and loses contact under cold weather conditions. Only second order data analysis unambiguously revealed this difficulty, arguing strongly for near real-time second order analysis of data in future tests.

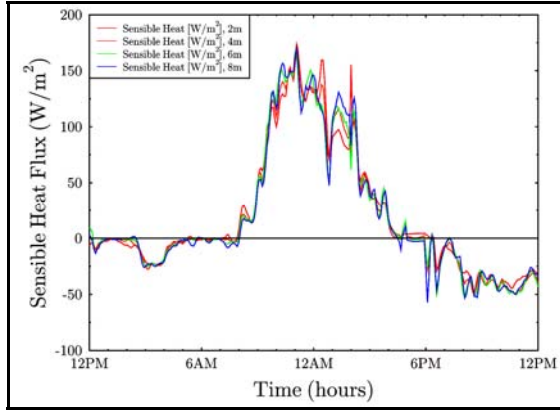


(Figure 63-November 9<sup>th</sup>)

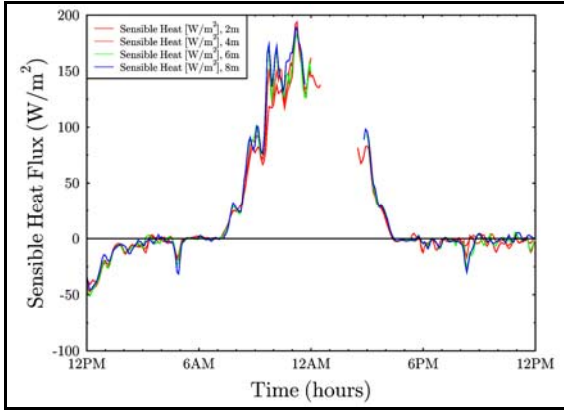


(Figure 64-November 10<sup>th</sup>)

Figures 63 and 64. Fifteen-minute averaged sensible heat fluxes for November 9<sup>th</sup> and 10<sup>th</sup> for 2.5, 4.5, 6.5, 8.5 m sonic anemometer levels.

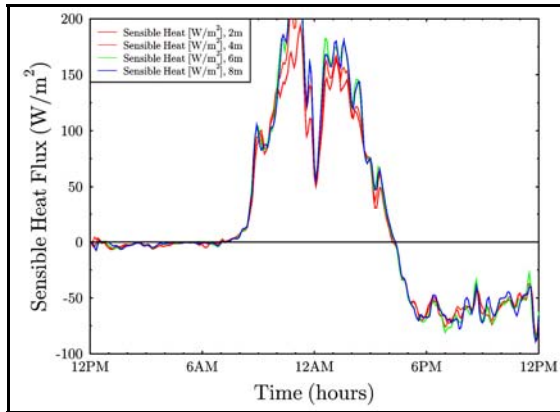


(Figure 65-November 11<sup>th</sup>)

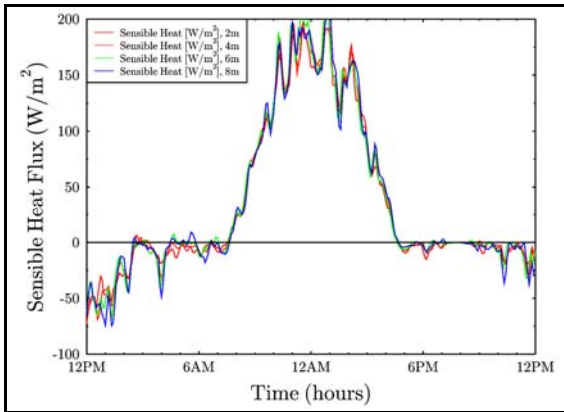


(Figure 66-November 12<sup>th</sup>)

Figures 65 and 66. Fifteen-minute averaged sensible heat fluxes for November 11<sup>th</sup> and 12<sup>th</sup> for 2.5, 4.5, 6.5, 8.5 m sonic anemometer levels.

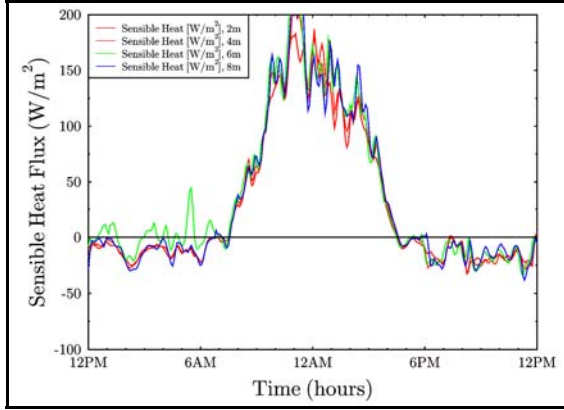


(Figure 67-November 13<sup>th</sup>)

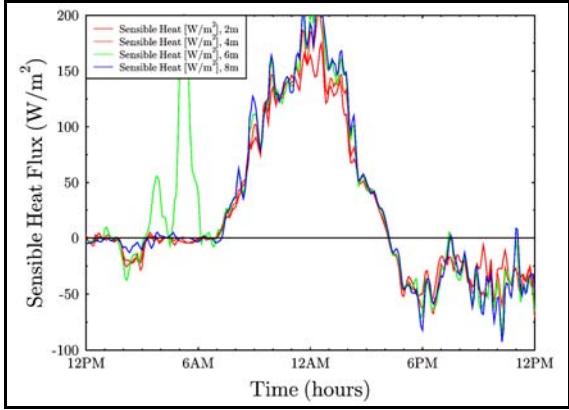


(Figure 68-November 14<sup>th</sup>)

Figures 67 and 68. Fifteen-minute averaged sensible heat fluxes for November 13<sup>th</sup> and 14<sup>th</sup> for 2.5, 4.5, 6.5, 8.5 m sonic anemometer levels.

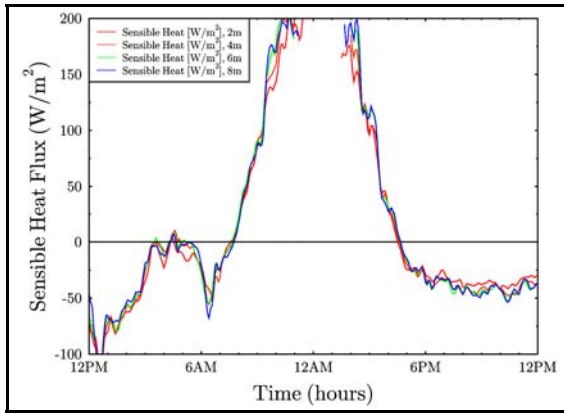


(Figure 69-November 15<sup>th</sup>)

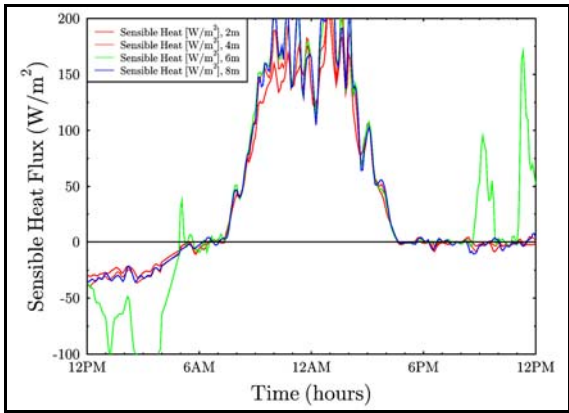


(Figure 70-November 16<sup>th</sup>)

Figures 69 and 70. Fifteen-minute averaged sensible heat fluxes for November 15<sup>th</sup> and 16<sup>th</sup> for 2.5, 4.5, 6.5, 8.5 m sonic anemometer levels.

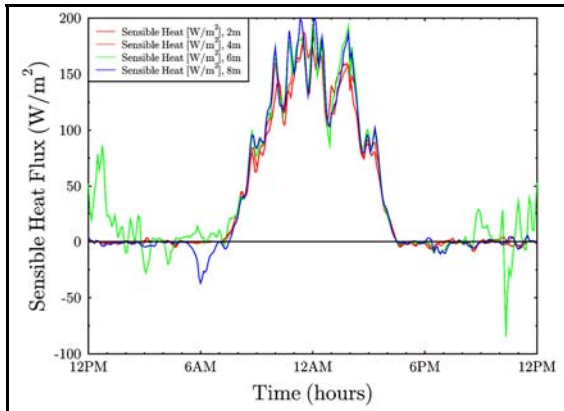


(Figure 71-November 17<sup>th</sup>)

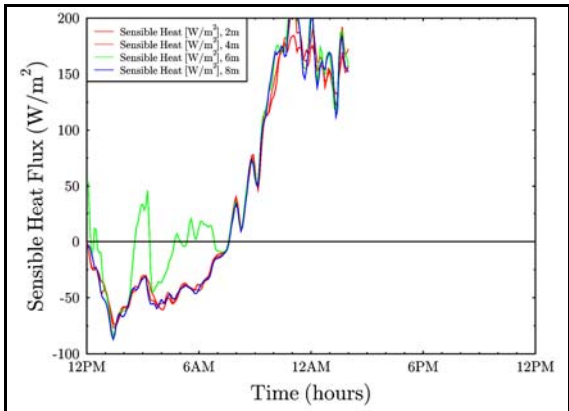


(Figure 72-November 18<sup>th</sup>)

Figures 71 and 72. Fifteen-minute averaged sensible heat fluxes for November 17<sup>th</sup> and 18<sup>th</sup> for 2.5, 4.5, 6.5, 8.5 m sonic anemometer levels.

The sensible heat flux data appears to show a similar behavior for the 6.5 m sensor as the momentum flux plots, deviating from the other sensors on the same nights during the same periods. Aside from these deviations, however, the heat flux data appear to indicate a significant amount of consistency between the sensors, even the 6.5 m sensor outside the cold intervals, particularly during the daytime.

We observed several periods where the sensible heat flux at night was near zero, as well as several intervals of large heat flux, which are interesting from the standpoint of stable boundary layer (SBL) studies. We thus would expect to find considerable variations in the stability conditions present during the measurement period.

---

#### 4. Temperature and Wind Spectra and Turbulence Computations

---

The spectral properties of temperature and wind provide additional information regarding the structure of atmospheric fluctuations. The primary region of interest in the spectrum is the inertial subrange, which is the cascade region between the outer scale source range and the inner scale dissipation region. Standard theories of atmospheric turbulent motions have the spatial spectra of atmospheric parameters typically exhibiting a  $\kappa_1^{-5/3}$  spectral dependence characteristic of one-dimensional stationary tower measurements in this spectral subrange. Here,  $\kappa_1$  is the one-dimensional stream wise spatial frequency. Assuming a mean horizontal wind speed  $U$  during a set of measurements, the cyclic temporal frequency,  $n$ , produced by the collections can be converted to spatial frequency by means of the transformation  $\kappa_1 = 2\pi n / U$ .

Our main focus in this study has been on the fluctuations of horizontal wind speed ( $u'$ ) about the mean  $U$ , vertical wind speed fluctuations ( $w'$ ) about an assumed zero mean vertical wind speed, and temperature fluctuations ( $T'$ ) about the mean  $T$ . From the spectral power density of  $u'$ ,  $S_{uu}(n)$ , the kinetic energy dissipation rate can be determined. In the inertial subrange

$$\varepsilon = \frac{2\pi}{U} \left[ \frac{\langle n^{5/3} [2S_{uu}(n)] \rangle}{\alpha} \right]^{3/2}, \quad (2)$$

where  $\varepsilon$  is the energy dissipation rate,  $\alpha$  is the Kolmogorov constant equal to 0.53,  $U$  is the mean streamwise wind speed, and the numerator in angle brackets is the compensated spectral intensity that is to be averaged over the inertial subrange. The factor of 2 that appears in the bracketed factor of equation 2 above is not seen in some common developments (e.g., Kaimal et al., 1972), where spectra are defined over a single-sided domain. Our development below, which relies upon the double-sided domain of the FFT, requires that we add an additional factor of 2 to correctly calculate the spectral power density. Knowledge of the dissipation rate provides an



estimate of the inner scale of turbulence. An important intermediate scaling parameter is the Kolmogorov scale,

$$\eta_k = \sqrt[4]{\nu^3 / \varepsilon}, \quad (3)$$

with  $\nu$  the kinematic viscosity,  $\nu = \mu / \rho$ , where  $\mu$  is the dynamic viscosity (e.g., List, 1951) and  $\rho$  is the atmospheric density. Dynamic viscosity can be computed as,

$$\frac{\mu}{\mu_0} = \frac{T_0 + C}{T + C} \left( \frac{T}{T_0} \right)^{3/2}, \quad (4)$$

with  $T_0 = 291.16$  K,  $C = 120$  K,  $\mu_0 = 1.827 \times 10^{-4}$  g/cm/s. Given  $\eta_k$ , the inner scale is computed as  $\ell_o = 7.41 \eta_k$  (Wyngaard, 1973).

A similar statistically-based analysis can be applied to the temperature power spectrum. Ishimaru (1978) bases his analysis on fluctuations of the potential temperature,  $\theta$ . Beland (1993) writes a general structure function as

$$D_R(\vec{r}) = \left\langle [R(\vec{x} + \vec{r}) - R(\vec{x})]^2 \right\rangle = 2\sigma_R^2 [1 - \rho_R(\vec{r})], \quad (5)$$

where  $\sigma_R^2$  is the variance of parameter  $R$ , and  $\rho_R(\vec{r})$  is the autocorrelation. The power spectrum for variable  $R$  is the Fourier transform of  $\sigma_R^2 \rho_R(\vec{r})$ .

An atmospheric conservative passive additive scalar parameter  $R$  (e.g., temperature and refractive index fluctuations) has the structure function

$$D_R(\vec{r}) \approx C_R^2 r^{2/3} \text{ for } l_o \ll r \ll L_o, \quad (6)$$

where turbulence is assumed homogeneous and isotropic. The quantities  $C_R^2$  are termed structure parameters. Here, the parameters  $l_o$  and  $L_o$  are the respective inner and outer scales of turbulence. Near the earth's surface, the inner scale is generally on the order of several millimeters, while the outer scale is on the order of several meters. As noted previously, between these scales is the so-called inertial subrange.

Variations of refractive index near the earth's surface are primarily due to temperature fluctuations. Effectively,

$$C_n^2 = (\partial n / \partial T)^2 C_T^2, \quad (7)$$

$$\frac{\partial n}{\partial T} = -78.2 \times 10^{-6} \frac{P}{T^2}. \quad (8)$$

From this basis, we note that the Kolmogorov spectrum of turbulence, a spectral form assuming zero inner scale and infinite outer scale, is given by,

$$\Phi_n(\kappa) = \beta_n C_n^2 \kappa^{-11/3}, \quad (9)$$

with  $\beta_n = 0.033$  (Tofsted, 2000). This spectral form is the three-dimensional spectrum of refractive index fluctuations. A one-dimensional form of this spectrum is found by integration:

$$V_n(\kappa_1) = \int_0^\infty \Phi_n(\sqrt{\kappa_1^2 + \kappa_r^2}) 2\pi \kappa_r d\kappa_r \approx \frac{6\pi}{5} \beta_n C_n^2 \kappa_1^{-5/3}, \quad (10)$$

in the inertial subrange portion of the spectrum ( $1/L_o \ll \kappa_1 \ll 1/\ell_o$ ), and  $\kappa_1$  is the one-dimensional spectral variable.  $V_n(\kappa_1)$  can also be related to the 3-D spectrum  $\Phi_n(\kappa)$  through the relation (Tatarskii's equation (1.27), 1961),

$$\Phi_n(\kappa) = -\frac{1}{2\pi \kappa} \frac{dV_n}{d\kappa}.$$

The governing frequency variable in the one-dimensional spectrum is envisioned by Tatarskii via: "If in a homogeneous and isotropic field we single out any straight line and consider the values of the field only along this line, then as a result we obtain a random function of one variable  $x$ , to which we can apply all the results pertaining to stationary random functions." From our tower measurements we make the assumption that the wind speed is relatively uniform over the 15-minute averaging period. These considerations then lead to a frequency variable corresponding to the streamwise spatial frequency component  $\kappa_1 = 2\pi n/U$  associated with tower data.

Because of their close connection at visible and IR frequencies, the temperature and refractive index spectra will take roughly the same form as long as we confine our considerations to those portions of the electromagnetic spectrum. Therefore, the value of  $C_n^2$  should theoretically be derivable from the tower temperature spectra. The only restriction is that when tower measurements are used, the spectra produced are averaged over the integration period of the tower measurements, as opposed to scintillometer measurements, which use spatial integration to obtain an average result. To find the appropriate connection we must use the auxiliary relation between the one-dimensional temperature spatial spectral density  $V_T$  and the temperature temporal frequency spectral density  $S_{TT}$ :  $\kappa_1 V_T(\kappa_1) = f S_{TT}(f)$ , where  $f$  is the temporal frequency [Hz] of the tower sensed spectral power density. Because of numerical peculiarities of the tower data FFT procedure,  $S_{TT}(f) = \Delta T \Theta(+f) \Theta(-f)$ , where  $\Delta T = N/R$ , the total integration time equal to the number of samples  $N$  in the FFT divided by the data acquisition rate  $R$  (20 Hz for these runs), and the FFT  $\Theta$  itself defined as

$$\Theta(f = lR/N) = \frac{1}{N} \sum_n T_n' W_{\ln}^N, \quad (11)$$

with “twiddle” factors  $W_{\text{in}}^N$ , and the product  $\Theta(+f)\Theta(-f)$  identified as the transformed equivalent of the autocorrelation function (e.g., equation. (33) of Tofsted, 2001). The estimate of the  $C_n^2$  is therefore given by,

$$C_n^2 = (\partial n / \partial T)^2 C_T^2 = (\partial n / \partial T)^2 \frac{5}{6\pi \beta_n} \left( \frac{2\pi}{U} \right)^{2/3} \langle f^{5/3} S_{TT}(f) \rangle. \quad (12)$$

Note here that  $S_{TT}(f)$  is a two-sided spectrum, again, as opposed to the single-sided spectra normally considered in some parts of the literature (e.g., Panofsky and Dutton, 1984; Kaimal et al., 1972).

The temperature power spectrum may also be used to estimate the dissipation rate of fluctuations of virtual temperature, parameter  $N_\theta$ . In the near surface atmosphere, the variables of temperature,  $T$ , and virtual temperature,  $\theta$ , are essentially identical. From Ishimaru (1978) we can therefore write the adapted form  $C_T^2 \approx C_\theta^2 = b N_\theta / \varepsilon^{1/3}$ , relating the temperature structure parameter to the dissipation rate and the temperature fluctuation dissipation rate, and where  $b$  is considered a universal constant.  $N_\theta$  is also considered to vary linearly relative to the square of the vertical temperature gradient.

Our primary limitation to exploiting these results is the nature of the observed spectra. As an example, hourly spectral plots from November 9<sup>th</sup> are shown in the next 24 figures (figures 73 through 96 on the following pages). In each plot there are three spectra: in red is the streamwise horizontal wind speed fluctuation spectrum, in orange is the vertical wind spectrum, and in blue is temperature spectrum. Also plotted are three lines corresponding to -5/3rds, -4/3rds, and -3/3rds power laws. As expected, the spectra of vertical wind begin at points depressed below the streamwise wind spectra at low frequency and eventually appear to nearly coincide with the streamwise spectra at high frequency. However, the behaviors of these two spectra are not consistent throughout the day. For example, in the 2:30, 3:30, 7:30–11:30, and 20:30–23:30 hour plots, the vertical and horizontal wind spectra observed are consistent with a 4/3rds vertical-to-horizontal ratio that would be expected from theory. However, the 16:30 and 17:30 plots show high frequency vertical wind spectra that are distinctly below the horizontal wind spectra.

The optical turbulence values estimated from the 2.5 m sonic anemometer data that are coplotted on the half-hour with measured turbulence data in figures 33 through 42 may be used to assess the utility of this estimation technique. Several observations may be made about this comparison. First, the predicted 2.5 m  $C_n^2$  values from the sonic data appear to be consistently low compared to the 1–2 km scintillation measurements, for the 2 m level and often for the 4 m level. Part of this difference can be explained by the height and location differences of the sonic anemometer and scintillometer sensors, and part must be due to the point time averaging of the sonic versus the spatial and temporal averaging applied to the scintillometer data, but the factor of 2 seems large. Certainly this would not explain why the results are also often below the 4 m

scintillometer measurements as well. Further analysis of the terrain profiles may reveal a region where the LOS is closer to the surface near the center of the path, where the weighting function of the scintillometers reaches a maximum.

We had expected that it would be the two southern scintillometers that would register higher levels than the two northern instruments. The reason was that a very low “ridgeline” extended out some distance from the 500 m tower area into the region between the 0–1 km scintillometer transmitters and receivers. Indeed, some difficulty was experienced selecting the proper point so that LOS could be established. No similar problem was experienced on the 1–2 km paths. Contrarily, the 1–2 km  $C_n^2$  values appeared to be a factor 2 stronger than the values along the 0–1 km paths.

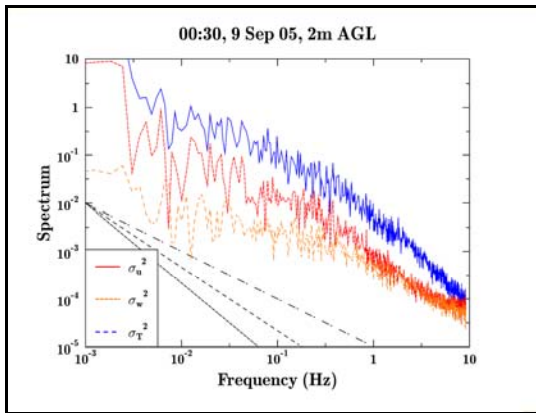


Figure 73

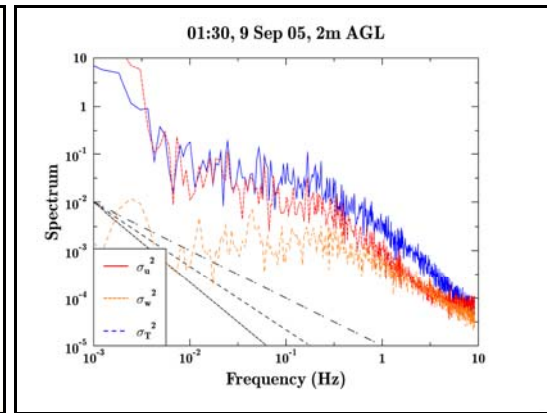


Figure 74

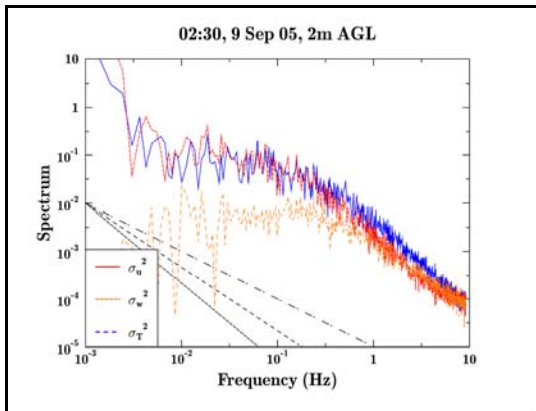


Figure 75

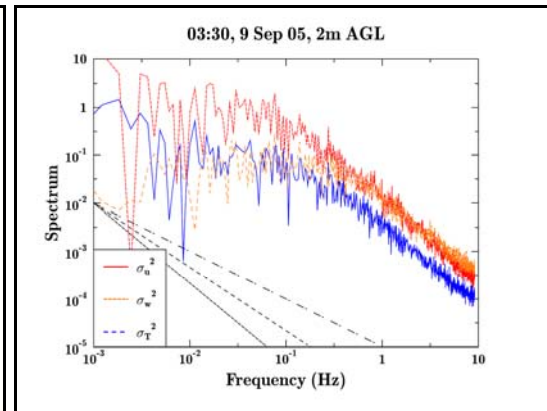


Figure 76

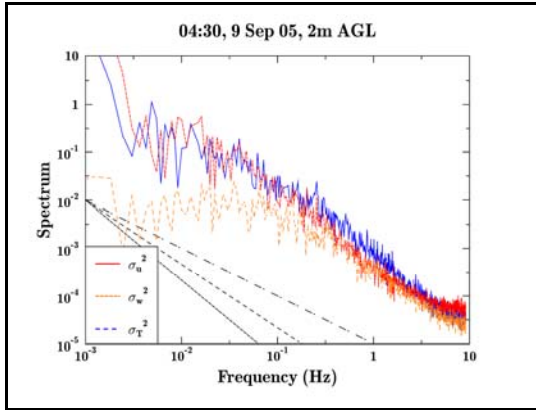


Figure 77

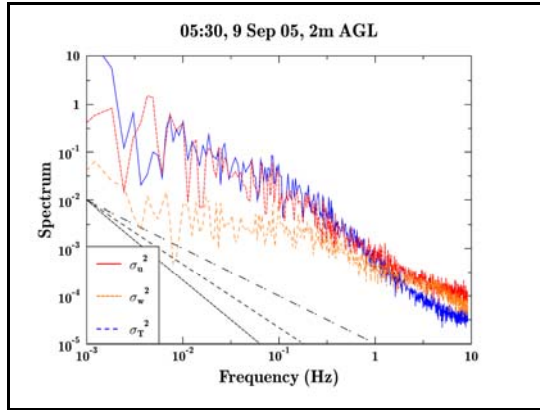


Figure 78

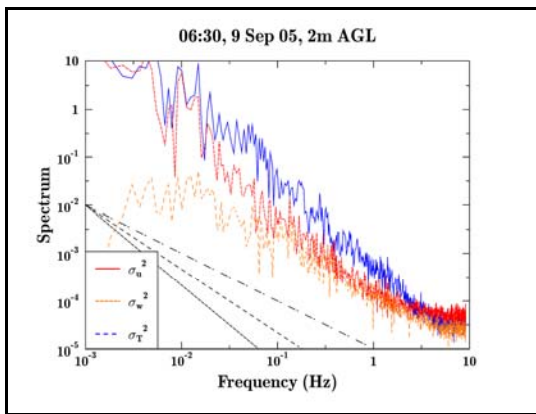


Figure 79

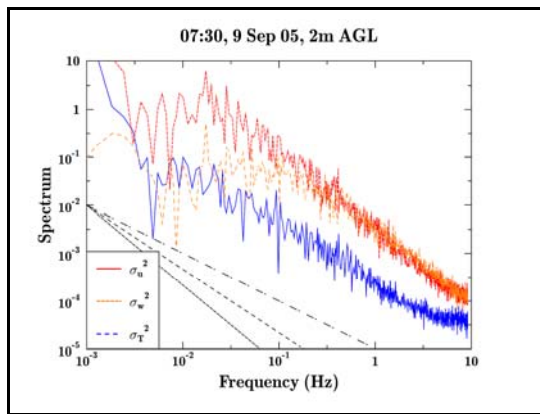


Figure 80

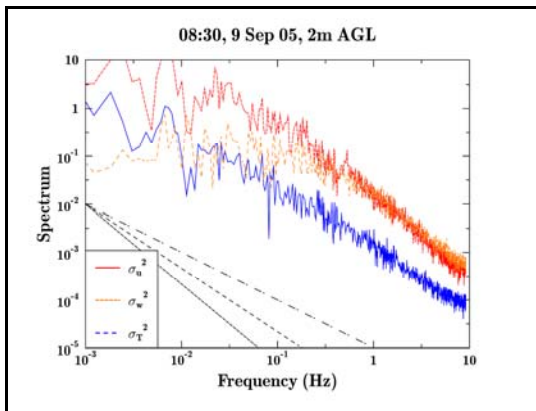


Figure 81

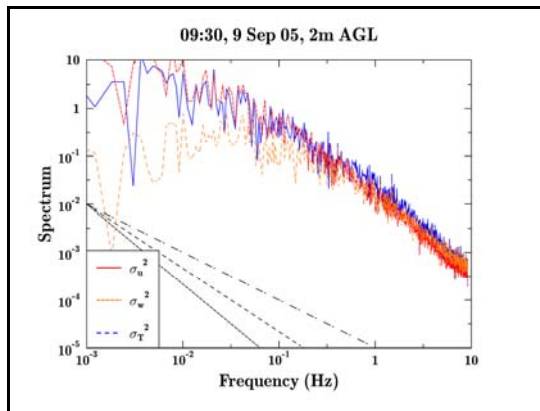


Figure 82

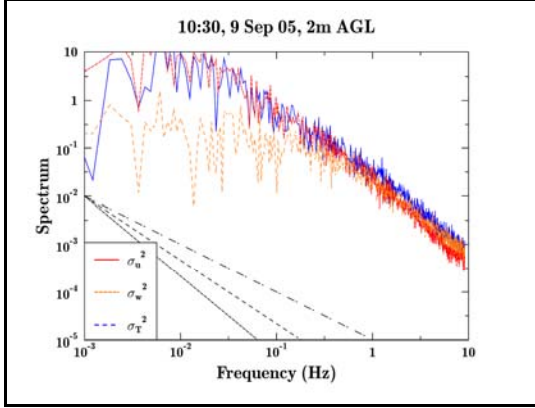


Figure 83

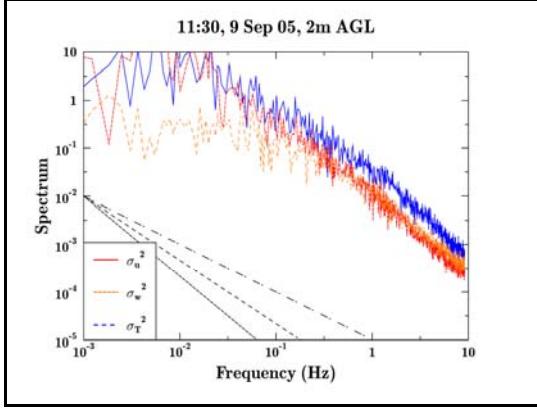


Figure 84

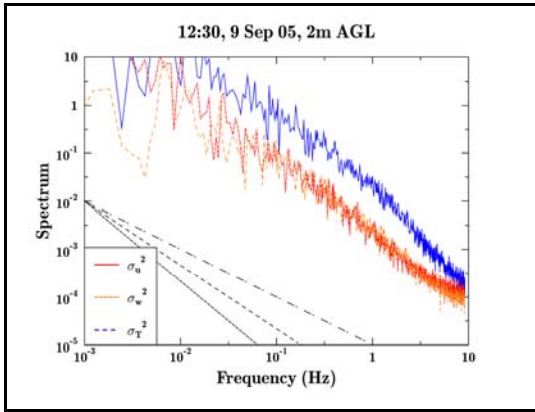


Figure 85

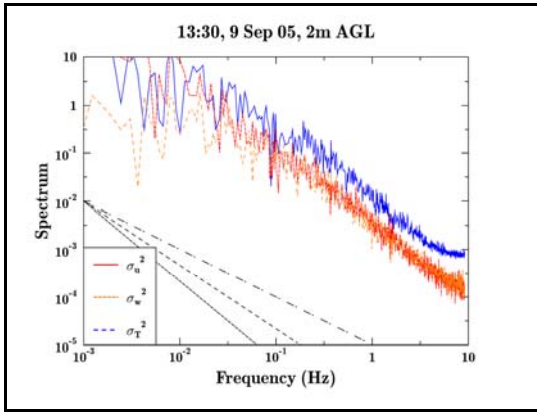


Figure 86

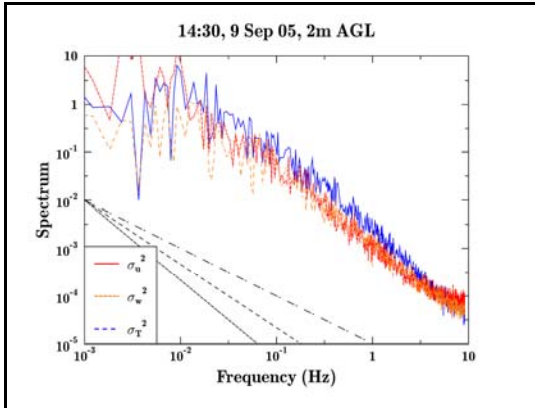


Figure 87

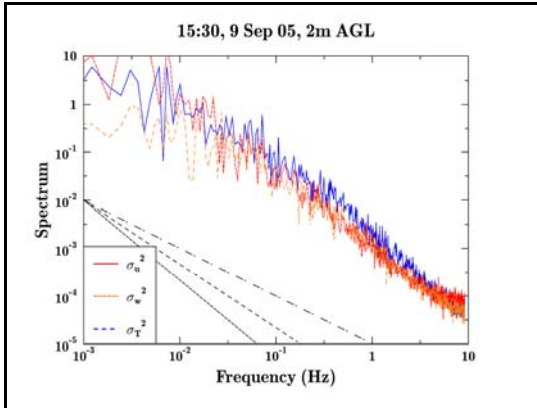


Figure 88

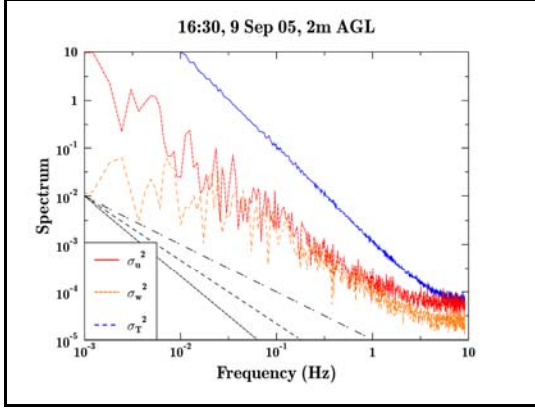


Figure 89

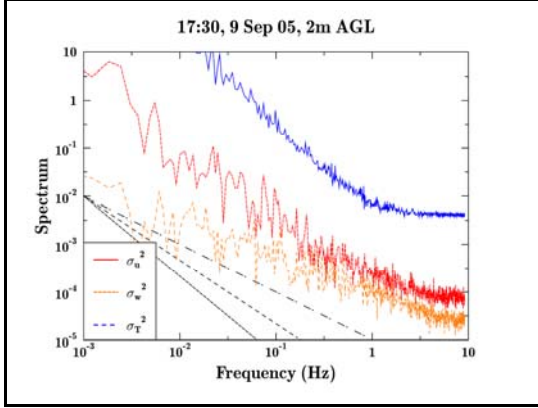


Figure 90

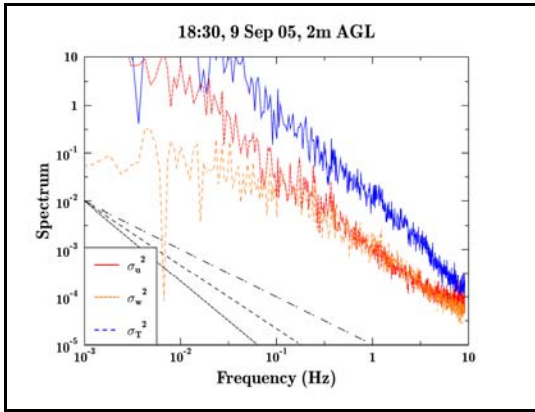


Figure 91

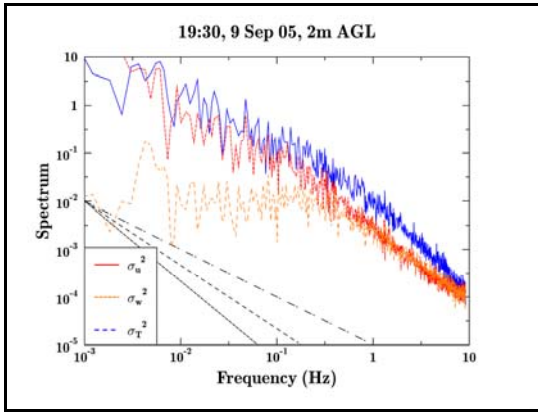


Figure 92

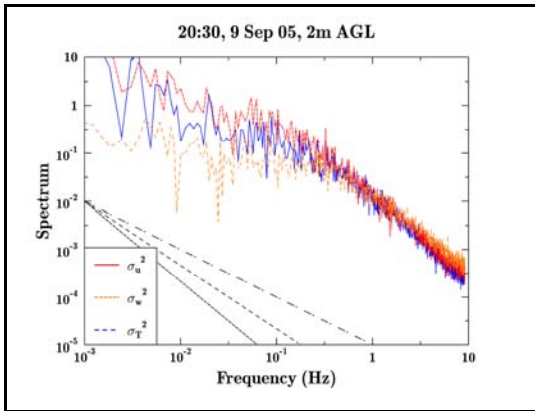


Figure 93

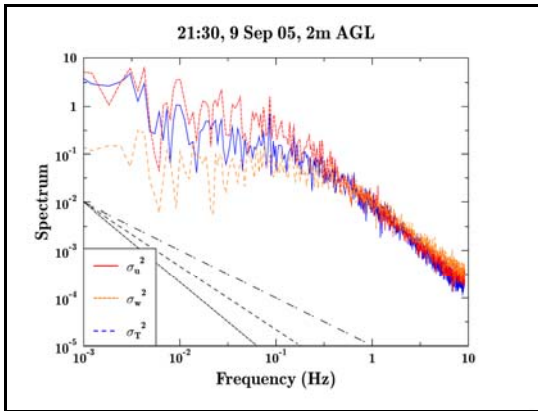
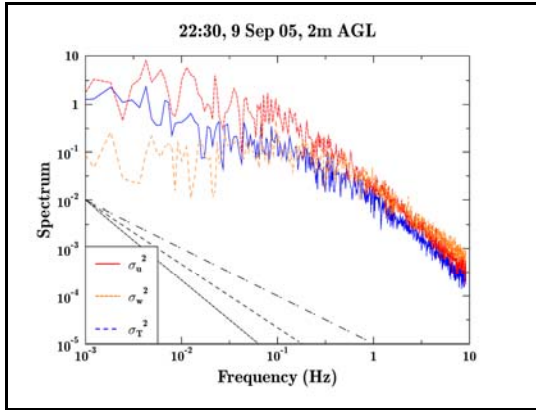
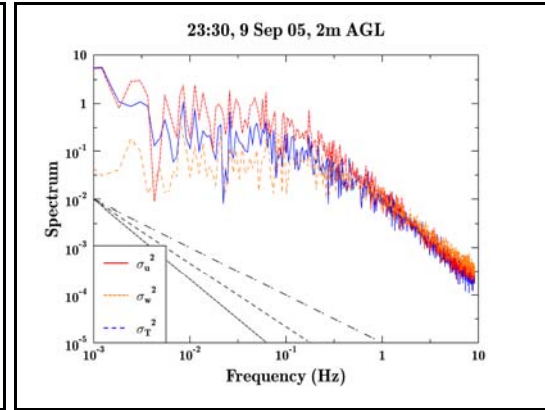


Figure 94





**Figure 95**



**Figure 96**

Figures 73 through 96. Hourly 15-minute-integration spectra of horizontal (u, red) and vertical (w, orange) wind, and temperature (blue) fluctuations of 9 November.

The vertical wind speed fluctuation spectrum had no observational data with which it might be directly compared in this experiment. However, the vertical fluctuation spectrum data can be put to use in comparisons with spectral behavior that is expected from theory. Of perhaps greatest interest are cases where the inertial subrange behavior does not appear to follow the  $-5/3$  power law rule for the horizontal and/or temperature spectra. These exceptional behaviors seem to follow several different patterns. In one pattern, the entire subrange spectrum may not exhibit the  $-5/3$  slope. This is seen, for example, in the vertical wind spectrum of the 17:30 graph. Another behavioral pattern is an inconsistency of aliasing effects. The 20 Hz sampling rate will yield a Nyquist frequency of 10 Hz, with the associated aliasing of higher frequency energy into spectral components below 10 Hz. In one instance, the aliasing effect appears relatively minor in the 18:30 spectrum, where the energies at the 10 Hz frequency are  $10^{-4.3}$ . In a contrasting example, aliasing is a major effect in the temperature spectrum of the 13:30 graph where the spectral energy is roughly  $10^{-3.1}$ .

An analysis of the noise spectrum of the RM Young sonic anemometers must acknowledge the fact that these devices only report wind and temperature data to 2 digits of accuracy after the decimal point. Therefore, the reported values have a random  $\pm 0.005$  unit uniform distribution of error. The spectrum associated with this error has been analyzed and displays a magnitude of approximately  $10^{-6}$  with a white noise characteristic shape. This is roughly equivalent to (within about a factor of 2) the variance of the error ( $0.01^2/12$ ) divided by the sampling rate (20 Hz). This value is well below the minimum values of the spectra plotted in figures 73–86. Therefore, the high frequency spectral flattening is not a sensor noise floor effect, even at the lowest spectral energies. It also does not appear to be due to excessive aliasing. The transition of aliasing seems to be very rapid in many of the figures (e.g., figures 85 and 86), yet appears extended in some cases (e.g., figures 80 and 86). Since these cannot be due to roundoff effects they are perhaps due to the analog processing limitations of the sensor at low wind speeds. The times when this effect is the most pronounced apparently correspond to mean winds below 2 m/s.



The worst cases apparently occur when the wind speed is approximately 0.5 m/s, regardless of the time of day.

It should be noted that, although the highest frequencies seem to show the potential for corruption due to unknown sources, the frequency range between about 1/3 Hz and 3 Hz appears to consistently show nearly log-linear form, even if this spectral dependence does not exactly match a  $-5/3$  theoretical dependence expected. The implications for SBL studies is that regardless of the disturbance of the vertical profile due to the stability, the spectra appear stable.

---

## 5. Conclusion

---

The NATO RTG-40 Active Imager Land Field Trials, conducted at the WSMR HELSTF range, represent the type of complex measurement program that can be accomplished given the mutual support and cooperation of coordinated agencies. The success of this program will lead to improved modeling of active imager systems by NATO countries and the advance of this promising technology.

At the same time, ARL has obtained a valuable data resource that shows the promise of revealing various aspects of diurnal patterns of structure within the surface layer atmosphere of a desert environment. Initial analysis has shown the quality of the sonic anemometer data taken. The consistency of the vertical fluxes of heat and momentum between different tower levels indicates that except for certain cold weather conditions the sensors were performing accurately. Results also indicate an effective method is available to estimate the refractive index structure parameter,  $C_n^2$ . The sonic anemometer also may be sufficient to characterize the surface layer, as it seems well suited to evaluation of the sensible heat flux, momentum flux, and spectral fluctuation properties of temperature and wind. Such properties are the basis for characterizing the dynamic similarity state of the surface layer (at least under daytime conditions). Further analyses using this data set are recommended, and ongoing, but for purposes of closure for this report, the analysis has been restricted to the results presented.

---

## References

---

- Beland. Propagation through Atmospheric Turbulence. Chapter 6 of *The Infrared Handbook*, Wolfe, W.L., Zissis, G. J., Eds; ERIM: Ann Arbor, MI, 1989.
- Ishimaru, A. *Wave Propagation and Scattering in Random Media. Volume 2*; Academic Press: New York, 1978.
- Kaimal, J.C.; Wyngaard, J.C.; Izumi, Y.; Cot'e, O.R. Spectral Characteristics of Surface-Layer Turbulence. *Q. J. Roy. Met. Soc.* **1972**, 98, 563-589.
- List, R.J., *Smithsonian Meteorological Tables*, Smithsonian Inst., Washington, DC, 1951.
- Ludeman, L.C., *Fundamentals of Digital Signal Processing*, J. Wiley & Sons, New York, 1986.
- Panofsky, H.A., and J.A. Dutton, *Atmospheric Turbulence: models and methods for engineering applications*, J. Wiley & Sons, New York, 1984.
- Tatarskii, V.I. *Wave Propagation in a Turbulent Medium*, Silverman, R.A., Translator; McGraw-Hill Book Company, Inc.: New York, 1961.
- Tofsted, D. H. *Turbulence Simulation: On Phase and Deflector Screen Generation*; ARL-TR-1886; U.S. Army Research Laboratory: White Sands Missile Range, NM, 2001.
- Tofsted, D. H. *Turbulence Simulation: Outer Scale Effects on the Refractive Index Spectrum*; ARL-TR-348; U.S. Army Research Laboratory: White Sands Missile Range, NM, 2000.
- Vickers, D.; Mahrt, L. The Cospectral Gap and Turbulent Flux Calculations. *J. Atmos. and Ocean. Tech.* **2003**, 20, 660-672.
- Wyngaard, J. C. On Surface Layer Turbulence. Chapter 3 of *Workshop on Micrometeorology*, Haugen, D. A., Ed.; American Meteorological Society: Boston, MA, 1972.

---

## Appendix: Scintillometer Calibrations

---

Calibration of the four Model IV-L, Lockheed Atmospheric Scintillometer, were performed both pre and post RTG-40 test. These units (most are circa era 1986 manufacture) were properly cleaned, aligned, and adjusted optically, and an electrical calibration was carefully performed. The instruments are designed to operate over ranges of 900 to 1200 m, measuring  $C_n^2$  over a range of  $1 \times 10^{-12}$  to  $1 \times 10^{-16} \text{ m}^{-2/3}$ .

The electrical calibration was performed in accordance with manufacturer's guidance, using a voltage standard and a precision voltage meter. Since calibration parameters were set to the manufacturer's specifications prior to the RTG-40 test, the following table lists post calibration values only. The voltages represent alignment drift for each adjustment required during voltage calibration for each of the four receivers. As shown in table A-1, Scintillometer Serial Number 1 (4 m level, facing South during test) showed a deviation of + 0.9% from manufacturers specifications; Scintillometer Serial Number 2 (2 m level, facing North during test) showed a deviation of +1.3% from manufacturers specifications; Scintillometer Serial Number 10 (4 m level, facing North during test) showed a deviation of +1.6% from manufacturers specifications, and Scintillometer Serial Number 11 (2 m level, facing South during test) showed a deviation of +1.2% from manufacturers specifications. However, the output at the BNC connector, representing the actual  $C_n^2$  value recorded as data, showed deviations from the specified values of no more than +/- 0.2% across the calibration voltage range. Considering the following corresponding voltage to  $C_n^2$  equivalence; 1 volt =  $1 \times 10^{-12}$ , 0.1 volt =  $1 \times 10^{-14}$ , and 0.01 volt =  $1 \times 10^{-16}$ , then 0.002 volt equals  $\sim 1.6 \times 10^{-17} C_n^2$  error at low  $C_n^2$  periods. This is presumably small, but other problems are noted with the 4 m North sensor in the analysis section.

Table A-1. Alignment drift for each sensor.

Scintillometer Serial No. 1				
AGC Card	U1 A/D Before adjustment(Mfg. Spec. w/0.100VDC input – Nominal = 0.00VDC output)		Output Amp Adj. Before adjustment (Mfg. Spec. w/1.00VDC input – Nominal = 2.00Vdc output)	
	0.012 V		2.013V	
C <sub>n</sub> <sup>2</sup> Card	Input Amplifier Balance Before adjustment (Nominal = 0.00 +/-5 mv )	C <sub>n</sub> <sup>2</sup> voltage at BNC after adjustment (Nominal = 1.000)	Output Amplifier Adjust (Mfg. Spec. w/0.100VDC input – Nominal = 0.00VDC output)	Output Amplifier Adjust (Mfg. Spec. w/1.00VDC input – Nominal = 2.00VDC output)
	0.002V	1.000	0.000V	2.018V adj. no lower
Scintillometer Serial No. 2				
AGC Card	U1 A/D Before adjustment(Mfg. Spec. w/0.100VDC input – Nominal = 0.00VDC output)		Output Amp Adj. Before adjustment (Mfg. Spec. w/1.00VDC input – Nominal = 2.00Vdc output)	
	0.002 V		2.016V	
C <sub>n</sub> <sup>2</sup> Card	Input Amplifier Balance Before adjustment (Nominal = 0.00 +/-5 mv )	C <sub>n</sub> <sup>2</sup> voltage at BNC after adjustment (Nominal = 1.000)	Output Amplifier Adjust (Mfg. Spec. w/0.100VDC input – Nominal = 0.00VDC output)	Output Amplifier Adjust (Mfg. Spec. w/1.00VDC input Nominal = 2.00VDC output)
	0.006 V	0.998V	0.001V	2.027V
Scintillometer Serial No.10				
AGC Card	U1 A/D Before adjustment(Mfg. Spec. w/0.100VDC input – Nominal = 0.00VDC output)		Output Amp Adj. Before adjustment (Mfg. Spec. w/1.00VDC input – Nominal = 2.00Vdc output)	
	0.002 VDC		2.006VDC	
C <sub>n</sub> <sup>2</sup> Card	Input Amplifier Balance Before adjustment (Nominal = 0.00 +/-5 mv )	C <sub>n</sub> <sup>2</sup> voltage at BNC after adjustment (Nominal = 1.000)	Output Amplifier Adjust (Mfg. Spec. w/0.100VDC input – Nominal = 0.00VDC output)	Output Amplifier Adjust (Mfg. Spec. w/1.00VDC input Nominal = 2.00VDC output)
	0.006 V	1.002	0.002V	2.032V adj. no lower
Scintillometer Serial No. 11				
AGC Card	U1 A/D Before adjustment(Mfg. Spec. w/0.100VDC input – Nominal = 0.00VDC output)		Output Amp Adj. Before adjustment (Mfg. Spec. w/1.00VDC input – Nominal = 2.00VDC output)	
	0.002 V		2.024V	
C <sub>n</sub> <sup>2</sup> Card	Input Amplifier Balance Before adjustment (Nominal = 0.00 +/-5 mv )	C <sub>n</sub> <sup>2</sup> voltage at BNC after adjustment (Nominal = 1.000)	Output Amplifier Adjust (Mfg. Spec. w/0.100VDC input – Nominal = 0.00VDC output)	Output Amplifier Adjust (Mfg. Spec. w/1.00VDC input Nominal = 2.00VDC output)
	0.000V	0.999V	0.006V	2.011V adj. no lower

---

## Acronyms and Abbreviations

---

2-D	two dimensional
3-D	three-dimensional
AFRL	Air Force Research Laboratory
AGL	above ground level
AR	Army Regulations
ARL	U.S. Army Research Laboratory
ASCII	American Standard Code for Information Interchange
BIL	Burst Illumination Laser
CERDEC	Communications Electronics Research Development and Engineering Command
cm	centimeter
DASYS	Danish system
ELVISS	Enhanced Low light level and Visible Surveillance System
EOVAF	Electro-Optical Vulnerability analysis Facility
FFT	Fast Fourier Transform
FRS	Family Radio Service
ft	feet or foot
FWHM	Full Width at Half Maximum
GPS	Global Positioning System
HELSTF	High Energy Laser System Test Facility
HWY	Highway
Hz	hertz
ID	identification
IR	infrared
km	kilometer

LASSIE	Land-based Active System & Surveillance Image Enhancement
LGS	Laser Ground Safety
LOS	line-of-sight
LSTC	Laser System Test Center
m	meter
met	meteorological
MFS	Missile Flight Safety
MOA	memorandum of agreement
mrad	milliard
NATO	North Atlantic Treaty Organization
NIR	near infrared
nm	nanometer
NVESD	Night Vision and Electronic Sensors Directorate of CERDEC
OA	observation area
OD	optical density
ORD	Operational Requirements Document
PC	personal computer
PPE	personal protective equipment
RTG	Research Technology Group
s	second
SBL	stable boundary layer
SIM	Sensor Interface Module
SLAD	Survivability/Lethality Analysis Directorate
SOP	Standard Operating Procedure
SOP	Safety Operating Procedure
SQL	Structured Query Language
SWIR	Short-wave IR

TTL	transistor-transistor logic
U.K.	United Kingdom
UXO	unexploded ordinance
WSMR	White Sands Missile Range

NOTE: Also see abbreviations given in table 5 for reference points at test site.

---

## Distribution List

---

Distribution	Copies	Distribution	Copies
Army Research Laboratory Attn: AMSRD-ARL-D 2800 Powder Mill Road Adelphi MD 20783-1197	1 CD	Army Research Laboratory Attn: AMSRD-ARL-CI-EE (M. Bustillos) WSMR NM 88002-5501	2 CDs/2 HCs
Army Research Laboratory Attn: AMSRD-ARL-RO-EV (Dr. Bach) PO Box 12211 Research Triangle Park, NC 27009	1 CD/1 HC	Army Research Laboratory Attn: AMSRD-ARL-CI-EE (J. Yarbrough) WSMR NM 88002-5501	2 CDs/2 HCs
Army Research Laboratory Attn: AMSRD-ARL-CI-EE (Dr. Shirkey) WSMR NM 88002-5501	1 CD	Director, USA TRADOC Analysis Center Attn: ATRC-W (P. Blechinger) WSMR, NM 88002-5502	1 CD
Army Research Laboratory Attn: AMSRD-ARL-CI-EE (D. Hoock) Battlefield Envir Div WSMR NM 88002-5501	1 CD	Director, USA TRADOC Analysis Center Attn: ATRC-WA (L. Southard) WSMR, NM 88002-5502	1 CD
Army Materiel Systems Analysis Activity Attn: AMXSY-SC (J. Mazz) 392 Hopkins Road APG MD 21005-5071	1 CD/1 HC	US Army CRREL Attn: Dr. G. Koenig 72 Lyme Rd Hanover, NH. 03755	1 CD
US Army Night Vision & Electronic Sensors Directorate Measurement and Modeling Services Branch Attn: MSRD-CER-NV-MS-MMS- (J. Hixson) 10221 Burbeck Road Fort Belvoir, VA 22060-5806	1 CD/1 HC	Army Corps of Engineers Topographic Eengineering Center Data and Signature Analysis Branch Ft. Belvoir, VA 22060	1 CD
Army Modeling & Simulation Office DA G37 (DAMO-SBM) 400 Army Pentagon Washington, DC 20310-0450	1 CD	US Military Academy Dept of Mathematical Sciences Thayer Hall West Point, NY 10996-1786	1 CD
Army Research Laboratory Attn: AMSRD-ARL-CI-EE (D. Tofsted) WSMR NM 88002-5501	5 CDs/5 HCs	United States Military Academy Combat Simulation Laboratory (Dr. P. West) West Point, NY 10996	2 CDs
Army Research Laboratory Attn: AMSRD-ARL-CI-EE (Dr. O'Brien) WSMR NM 88002-5501	2 CDs/2 HCs	AFRL/IFOIL 525 Brooks Road Rome, NY 13441-4505	1 CD
Army Research Laboratory Attn: AMSRD-ARL-CI-EE (D. Quintis) WSMR NM 88002-5501	2 CDs/2 HCs	Air Force Weather Tech Lib 151 Patton Ave Rm 120 Asheville NC 28801-5002	1 CD
		HQ USAFA/DFLIB 2354 Fairchild Drive, Suite 3A10 USAF Academy, CO 80840-6214	1 CD



<b>Distribution</b>	<b>Copies</b>	<b>Distribution</b>	<b>Copies</b>
Tech Connect AFRL/XPTC Bldg 16, Rm 107 2275 D Street WPAFB OH 45433-7226	1 CD	Northrop Grumman Information Technology Melanie Gouveia 55 Walkers Brook Dr Reading MA 01867	1 CD
Dr. Andy Goroch Naval Research Laboratory Marine Meteorology Division, Code 7543 7 Grace Hopper Ave Monterey, CA 93943-5006	1 CD/1 HC	Northrop Grumman Information Technology Dr. Haig Iskenderian 55 Walkers Brook Dr. Reading, MA 01867	1 CD
U.S. Naval War College War Gaming Department (Code 33) 686 Cushing Road Newport, Rhode Island 02841-1207	1 CD	Anteon Corp. Mike Adams 46 Growing Rd Hudson, NH 03051	1 CD
Naval Postgraduate School J. D. Eagle OR/Er 1 University Circle Monterey, CA 93943	1 CD	SAIC Attn: Mr. Delgado 731 Lakepointe Centre Dr. O'Fallon, Ill 62269-3064	1 CD
Naval Postgraduate School R. K. Wood OR/Wd 1 University Circle Monterey, CA 93943	1 CD	Technical Reports Boulder Laboratories Library, MC 5 325 Broadway Boulder, CO 80305	1 CD
Naval Postgraduate School G. Schacher Dept. of Physics 1 University Circle Monterey, CA 93943	1 CD	NCAR Library Serials National Center for Atmospheric Research PO Box 3000 Boulder CO 80307-3000	1 CD
Naval Postgraduate School W. B. Maier II Dept. of Physics 1 University Circle Monterey, CA 93943	1 CD	U.S. Army Research Laboratory Attn: IMNE ALC IMS Mail & Records Mgmt Adelphi, MD 20783-1197	1 CD/1 HC
Ruth H. Hooker Research Library 4555 Overlook Ave, SW Washington, DC 20375	1 CD	Administrator Defns Techl Info Ctr Attn: DTIC OCP (V Maddox) 8725 John J Kingman Rd., Ste. 0944 Ft Belvoir, VA 22060-6218	1 CD
JWARS Attn: C. Burdick 1555 Wilson Boulevard, Suite 619 Arlington, VA 22209	1 CD	U.S. Army Research Laboratory AMSRD ARL CI OK TL Techl Lib 2800 Powder Mill Rd. Adelphi, MD 20783-1197	2 CDs
U.S. Army Research Laboratory AMSRD ARL CI OK TP Techl Lib APG, MD 21005	2 CDs	US Army Night Vision & Electronic Sensors Directorate Sensor Performance Branch Attn: AMSRD-CER-NV-MS-SP (J. Reynolds) 10221 Burbeck Road Fort Belvoir, VA 22060-5806	1 CD/1 HC

**Distribution****Copies**

US Army Night Vision & Electronic Sensors  
Directorate 1 CD/1 HC  
Sensor Performance Branch  
Attn: AMSRD-CER-NV-MS-SP (R. Espinola)  
10221 Burbeck Road  
Fort Belvoir, VA 22060-5806

US Army Night Vision & Electronic Sensors  
Directorate 1 CD/1 HC  
Sensor Performance Branch  
Attn: AMSRD-CER-NV-MS-SP (M. Friedman)  
10221 Burbeck Road  
Fort Belvoir, VA 22060-5806

Dr. R. Rasmussen 1 CD  
National Center for Atmospheric Research  
P.O. Box 3000  
Boulder, CO 80307-3000

Dr. E. Jacobs 1 CD/1 HC  
The University of Memphis  
Department of Electrical and Computer Engineering  
206 Engineering Science Bldg.  
Memphis, TN 38152-3180

Endre Repasi Special Order (1 CD)  
FGAN-FOM  
Research Institute for Optronics and Pattern Recognition  
Gutleuthausstrasse 1  
76275 Ettlingen  
Germany

Endre Repasi 1 CD  
FGAN-FOM  
Research Institute for Optronics and Pattern  
Recognition  
Gutleuthausstrasse 1  
76275 Ettlingen  
Germany

Luc Forand 1 CD  
DRDC Valcartier  
2459 Pie XI Blvd North  
Quebec, QC  
Canada G3J 1X5

**TOTAL****58 CDs and 22 HCs**

